



Universität
Zürich^{UZH}

Study of the rare decay $Z \rightarrow \tau^+ \tau^- \mu^+ \mu^-$

Master Thesis

Mathematisch-naturwissenschaftliche Fakultät
der
Universität Zürich

Fanqiang Meng

21-736-699

Adviser

Prof. Dr. Benjamin Kilminster,
Dr. Stefanos Leontsinis,
Dr. Arne Reimers

Zürich
February 2023

Abstract

The first study of the Z boson decaying to two tau and two muon leptons in proton-proton collisions is presented. The analyzed data set corresponds to an integrated luminosity of 138 fb^{-1} at a center-of-mass energy of $\sqrt{s} = 13 \text{ TeV}$ collected by the CMS detector at the Large Hadron Collider. The branching fraction of the $Z \rightarrow \tau^+ \tau^- \mu^+ \mu^-$ decay is measured in the muon decay mode of the tau lepton relative to the $Z \rightarrow \mu^+ \mu^- \mu^+ \mu^-$ decay and their ratio within a fiducial region is expected to be $0.902 \pm_{-3.212}^{+3.590} \text{ (stat.)} \pm_{-1.825}^{+1.574} \text{ (syst.)}$.

Contents

1	Introduction	1
1.1	The Standard Model	2
1.2	LFU and physics beyond the SM	3
2	The CMS experiment	4
2.1	The LHC and proton-proton collisions	4
2.2	The CMS detector	4
2.3	Coordinate system	5
2.4	The tracking system	6
2.5	Calorimeter	7
2.6	Muon system	8
2.7	Readout system	9
3	Datasets and simulated samples	10
4	Event reconstruction	12
4.1	Particle Flow	12
4.2	Primary vertex	13
4.3	Muon identification	14
5	Event selections	15
6	Background estimation	17
7	Systematics	20
7.1	Corrections to simulated samples	20
7.2	Systematic uncertainties	21
8	Signal extraction	24
8.1	Sensitivity to $Z \rightarrow 4\mu$	25
8.2	Expected signal sensitivity	25
8.3	Bias test and goodness of fit	27
9	Results	31
9.1	Acceptance and efficiency	31
9.2	Non-resonant factor	31
9.3	Branching fraction measurement	35
10	Summary	37
	References	A
A	Appendix	I
A.1	Isolation distributions	I
A.2	Systematics variations	I

A.3	Acceptance and efficiencies cross check	M
A.4	Additional kinematic distributions	M

List of Figures

1	Feynman Diagram of the $Z \rightarrow \tau^+ \tau^- \mu^+ \mu^-$ process.	1
2	Standard Model of particle physics.	2
3	Schematic view of the CMS detector with its components.	5
4	CMS coordinate system with the LHC circuit.	6
5	The relation between the polar angle and the pseudorapidity.	6
6	Schematic cross section through the CMS tracker.	7
7	Layout of the CMS Phase-1 pixel detector compared to the original detector layout.	7
8	Layout of one quadrant of CMS.	9
9	Schematic view of a transverse slice of the CMS detector.	12
10	The signal region and control regions for the ABCD method (a). The validation regions for the closure test (b).	17
11	Distributions and statistical uncertainties of isolation variables of the three muons with lower p_T in the opposite-sign and like-sign region.	18
12	Pre-fit four muon invariant mass distribution without and with the signal sample.	24
13	The normalized pre-fit four muon invariant mass distributions.	25
14	Background-only fit result for the $Z \rightarrow \mu^+ \mu^- \mu^+ \mu^-$ process.	26
15	Negative log-likelihood profile of the signal+background fit to the signal+background Asimov dataset.	26
16	The upper limits on the signal strength using the CL_s method with the signal+background Asimov dataset.	27
17	Bias check for toy models without signal ($r = 0$, left) and with signal ($r = 1$, right).	28
18	The distribution of the goodness-of-fit measure	28
19	Post-fit nuisance parameters, uncertainties, and impacts of the background-only fit. The 2016 pre-VFP and 2016 post-VFP eras are noted as 16a and 16b here for short.	29
20	Post-fit nuisance parameters, uncertainties, and impacts from fit on the signal+background Asimov dataset. The 2016 pre-VFP and 2016 post-VFP eras are noted as 16a and 16b for short.	30
21	Resonant and non-resonant four lepton final state processes.	32
22	Generator level four muon invariant mass distribution in the CMS fiducial region.	34
23	Distributions and statistical uncertainties of isolation variables of the three muons with lower p_T in the regions B and D.	I
24	Distributions and statistical uncertainties of isolation variables of the three muons with lower p_T filling in the same histograms.	I

25	Norminal and μ_R, μ_F varied four muon mass distributions for the $Z \rightarrow \tau^+ \tau^- \mu^+ \mu^-$ and $Z \rightarrow \mu^+ \mu^- \mu^+ \mu^-$ process.	J
26	Norminal and varied four muon mass distributions for the $Z \rightarrow \tau^+ \tau^- \mu^+ \mu^-$ process.	K
27	Norminal and varied four muon mass distributions for the $Z \rightarrow \mu^+ \mu^- \mu^+ \mu^-$ process.	L
28	Signal plus background pre-fit distributions for (a) the p_T of the four muon system, (b) the mass of Z_1 , (c) the mass of Z_2	M
29	Signal plus background pre-fit distributions for the distance ΔR between each muon pairs.	N
30	Signal plus background pre-fit distributions for the p_T, η, φ of each muon.	O
31	Background post-fit distributions for (a) the p_T of the four muon system, (b) the mass of Z_1 , (c) the mass of Z_2	P
32	Background only post-fit distributions for the distance ΔR between each muon pairs.	P
33	Background only post-fit distributions for the p_T, η, φ of each muon.	Q

1 Introduction

The standard model (SM) of particle physics [1–3] is a highly successful theory that describes the fundamental nature of matter and the fundamental forces that govern its interactions. One key feature of the SM is the division of leptons into three generations, each with the same gauge coupling. Thus, the gauge interactions are universal across generations. The only difference among them is the mass that results from the Yukawa coupling with the Higgs boson.

Despite the remarkable success, there are still many open questions. In particular, the lepton flavour non-universality is not confirmed nor disapproved by any deeper structure. This has led to questions of whether a more elaborate lepton flavour universality (LFU) may exist or whether there might be mechanisms for lepton flavour violation. The latter could manifest itself in some measurements as deviations from the SM predictions and hint at new physics beyond it.

One way to test the LFU is to study the vector boson decays to final states containing leptons and compare the branching fractions with different lepton flavours. The Compact Muon Solenoid (CMS) experiment [4] at the CERN Large Hadron Collider (LHC) [5] was the first to observe the rare decays of $Z \rightarrow J/\psi \ell^+ \ell^-$ [6] and $Z \rightarrow \ell^+ \ell^- \ell'^+ \ell'^-$ [7] and measure the branching fraction of $Z \rightarrow 4\ell$ [8] in proton-proton collisions, where ℓ includes electrons and muons. Yet the Z boson four leptonic decay including tau leptons has not been probed.

This thesis presents the first dedicated study of the $Z \rightarrow \tau^+ \tau^- \mu^+ \mu^-$ decay in the muon decay mode of the τ leptons, as shown in Fig. 1, and sets an upper limit on the branching fraction $\mathcal{B}(Z \rightarrow \tau^+ \tau^- \mu^+ \mu^-)$. The result not only contributes to untested Standard Model Effective Field Theory (SMEFT) Wilson coefficients [9] but also to the exploration of Z' and $L_\mu - L_\tau$ models [10, 11] of physics beyond the SM, in which τ leptons can experience stronger couplings. Finally, this channel is also a background to Higgs boson leptonic decays [12]. The rest of this chapter includes an elaborate description of the theoretical background.

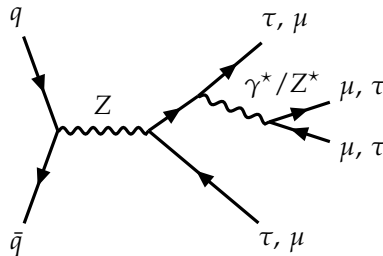


Figure 1: Feynman Diagram of the $Z \rightarrow \tau^+ \tau^- \mu^+ \mu^-$ process.

Chapter 2 introduces the CMS experiment and its data collection, followed by the datasets and simulated samples used in this work (Chapter 3). The reconstruction of the events

and physics objects from the data and simulation is explained in Chapter 4 focusing on muons. This analysis uses cut-based event selections and a data-driven estimation for backgrounds consisting of non-prompt muons, which are detailed in Chapters 5 and 6. Chapter 7 describes several corrections and systematic uncertainties. The signal yield is extracted from a binned maximum-likelihood fit to the data (Chapter 8) and the results are shown in Chapter 9. The thesis concludes in Chapter 10 with a short summary.

1.1 The Standard Model

The standard model of particle physics [1–3], as a gauge theory based on the $SU_C(3) \otimes SU_L(2) \otimes U_Y(1)$ symmetry group, describes interactions between all known elementary particles through the strong and electroweak forces. Shown in Fig. 2., the particles are classified as fermions with half-integer spins and bosons with integer spins, where spin refers to the particle’s intrinsic angular momentum. Each of them is accompanied by its antiparticle with the same mass but opposite physical charge.

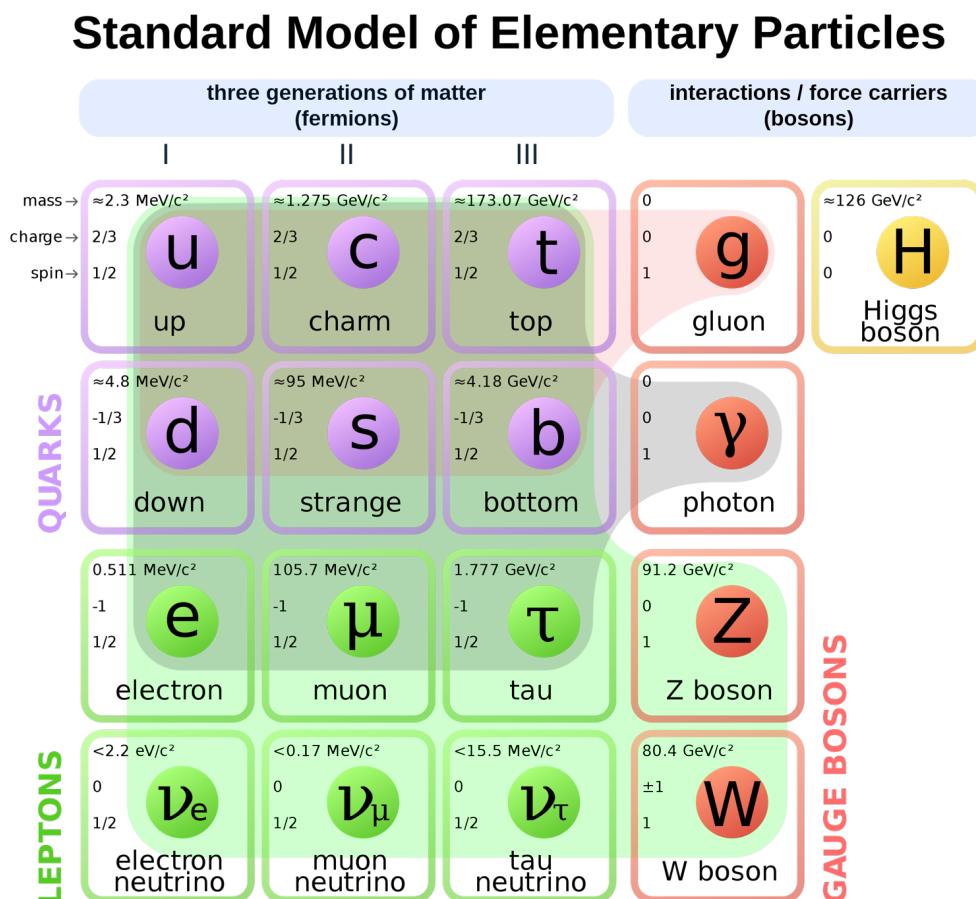


Figure 2: Standard Model of particle physics [13].

Fermions are categorized as quarks and leptons depending on whether they carry color charges. Quarks carry color charges and participate in the strong interaction. Quarks and leptons carry weak isospins and can interact via the weak interaction. Only quarks and

leptons that carry electromagnetic charges feel the electromagnetic force. Fermions are further divided into three generations, as shown in Fig 2. Since the physical charges are identical among the generations, the gauge forces are universal across generations while the only difference among them in the SM is the mass that increases with the generation. The τ lepton is the heaviest lepton.

The fundamental interactions in the SM are described via the exchange of the spin-1 gauge bosons. The strong interaction is mediated by massless gluons (g) and formulated by Quantum Chromodynamics (QCD). Because of the color confinement phenomenology, color-charged particles can not be isolated. Quarks and gluons must clump together to form composite colorless particles called hadrons and thus the process is called hadronization. The photon (γ) transmits the electromagnetic force and is massless. The Z and W bosons are the mediators of the weak force and are, however, massive. Mass terms for charged fermions and gauge bosons are forbidden in the SM Lagrangian because they violate the local gauge invariance. In the SM, the particles acquire mass through the Brout-Englert-Higgs mechanism [14–17], which predicted the so-called Higgs boson. The Higgs boson is the only scalar boson in the SM and was discovered in 2012 by the ATLAS and the CMS collaborations [18, 19].

1.2 LFU and physics beyond the SM

The charged lepton sector in the SM includes three copies with the same physics charge and gauge coupling except for the mass. Such a lepton flavour universality is not explained within SM yet and is still under examination from various measurements [20–26]. It leads to global symmetries which are not preferred by the locality. For example, the difference in the muonic and tauonic lepton number $L_\mu - L_\tau$ is conserved accidentally and anomaly-free in the SM. Thus, it can be gauged as a local $U(1)$ symmetry as an extension to the SM gauge group associated with a gauge boson called Z' [10, 11]. This $L_\mu - L_\tau$ model only couples to the second- and third-generation leptons. This model has gained increasing attention in recent years [27–37] as it could explain the measured value of the anomalous muon magnetic moment [38–42] with certain values of the Z' mass and coupling strength. The Z' could also mediate an interaction between dark matter and ordinary matter [43–46], which would make the bounds on the dark matter coupling strength from direct-detection experiments less stringent as the Z' considered here does not couple directly to quarks. Apart from particular new physics models, SMEFT four-lepton operators can also introduce lepton flavour violation and contribute to the decay studied in this analysis. These theory motivations make the Z boson four-lepton decays involving τ leptons important to explore.

2 The CMS experiment

This work is based on the data collected by the CMS experiment at the Large Hadron Collider (LHC) [5]. The LHC is a high-energy particle collider built by the European Organization for Nuclear Research (CERN) and designed to collide protons at a center-of-mass energy of 14 TeV. It is built in a circular tunnel with a circumference of 26.7 km. The machine was operated at a center-of-mass energy of 7 TeV from 2010 to 2011. After upgrades, the operating energy reached 13 TeV from 2015 to 2018.

2.1 The LHC and proton-proton collisions

The LHC uses protons and heavy-ions for collisions. For proton-proton (pp) collisions, the protons are accelerated in opposite directions in separate beam pipes inside the accelerator and are brought to the collision at a rate of 40 MHz, i.e., one collision every 25 ns, at four fixed interaction points along the circular path where the four main detectors located: CMS, ATLAS, LHCb, and ALICE. The two multipurpose detectors, CMS and ATLAS (A Toroidal LHC Apparatus) [47], are designed to explore the energy frontier of particle physics and study the standard model and physics beyond. The LHCb (LHC beauty) experiment [48] is a forward particle detector that mainly focuses on measurements of CP violation and B -meson physics. ALICE (A Large Ion Collider Experiment) [49] is dedicated to the study of heavy-ion collisions and the research of quark-gluon plasma.

A key parameter for the collider is luminosity [5]. The instantaneous luminosity $d\mathcal{L}/dt$ measures the ability of a particle accelerator to produce the required number of interactions and is the proportionality factor between the number of events per second dN/dt and the cross section σ as

$$\frac{dN}{dt} = \frac{d\mathcal{L}}{dt} \times \sigma. \quad (2.1)$$

In the LHC, the instantaneous luminosity, depending on several parameters such as the number of bunches and of protons in each bunch and the effective transverse area of the proton beam, is designed to be $10^{34} \text{ cm}^{-2} \text{ s}^{-1}$. Several inelastic collisions occurring in the same or adjacent bunch crossings will be superimposed on the event of interest. They are referred to as pileup events. The integrated luminosity \mathcal{L} measures the amount of data delivered by the LHC.

2.2 The CMS detector

The CMS is a general-purpose detector built to exploit the physics opportunities presented by the LHC. The rest of this chapter is a brief introduction to CMS, as shown in Fig. 3. The central feature of the CMS apparatus is a superconducting solenoid of 6 m internal diameter, providing a magnetic field of 3.8 T. Within the solenoid volume are a silicon pixel and strip tracker, a lead tungstate crystal electromagnetic calorimeter (ECAL), and a brass

and scintillator hadron calorimeter (HCAL), each composed of a barrel and two endcap sections. Forward calorimeters extend the pseudorapidity coverage provided by the barrel and endcap detectors. Muons are measured in gas-ionization detectors embedded in the steel flux-return yoke outside the solenoid. A more detailed description of the CMS detector can be found in Ref. [4].

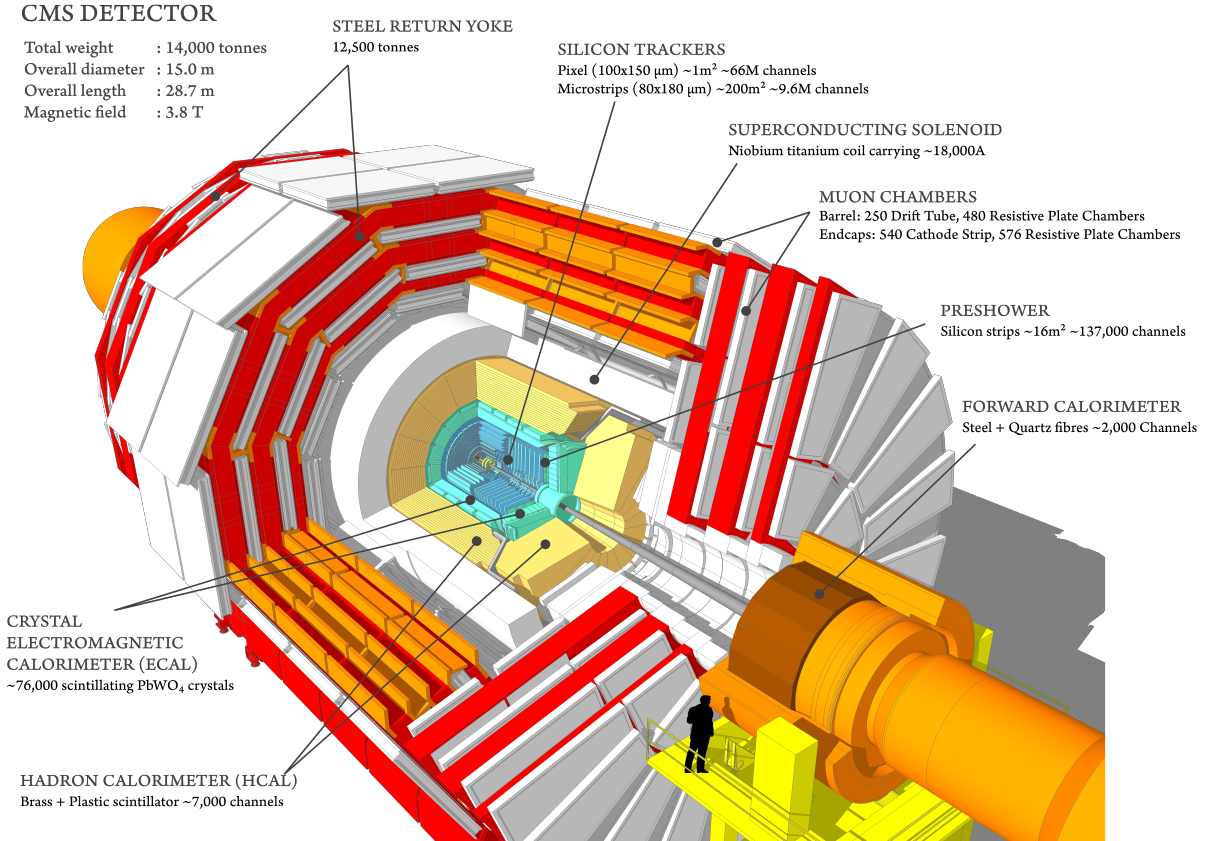


Figure 3: Schematic view of the CMS detector with its components [50].

2.3 Coordinate system

The CMS coordinate system to describe the position and kinematic of particles is shown in Fig. 4 and defined below. The origin of the coordinate system is set at the center of the interaction region. Viewed from above, the z -axis is counterclockwise tangential to the beam direction. The xy -axes form the transverse r plane with the x -axis pointing toward the center of the LHC ring and the y -axis pointing vertically upward. The momentum transverse to the beam direction, p_T , and the azimuthal angle ϕ are defined and measured in the r -plane. The ϕ is defined with respect to the x -axis. They are invariant with respect to the Lorentz boost along the z -axis. The polar angle related to the positive z -axis is denoted as θ . Instead of θ , the pseudorapidity variable $\eta = -\ln[\tan(\theta/2)]$ is used in the analysis because of the easier treatment when dealing with the Lorentz transformation for high-energy particles. Fig. 5 shows the relation between θ and η .

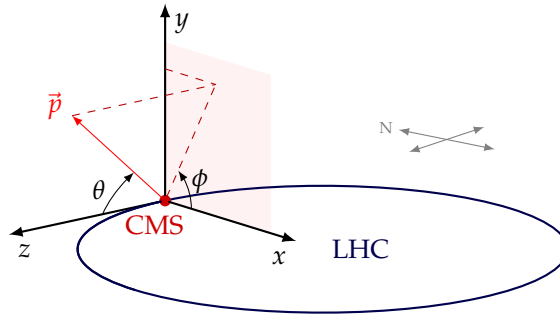


Figure 4: CMS coordinate system with the LHC circuit.

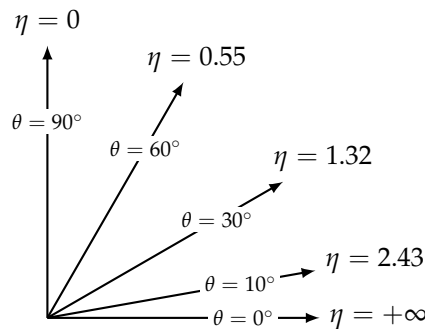


Figure 5: The relation between the polar angle θ and the pseudorapidity η .

2.4 The tracking system

The CMS tracking system consists of the innermost silicon pixel detectors and the silicon microstrip detectors and is crucial for track and vertex reconstructions [51]. When flying out, the charged particle ionizes the depleted p-n junction in the silicon detectors and produces signals (hits). Bathed in a co-axial magnetic field of 3.8 T provided by the outer solenoid, the trajectory of the charged particle is helical. Its bending direction determines the sign of the particle's charge and its curvature in the transverse plane is used to measure the p_T of the particle.

The tracker has a coverage of $|\eta| < 2.5$ and is symmetric about the z-axis. A schematic view of the tracker is shown in Fig. 6, where the green dashed lines group modules to each of the named tracker subsystems. At the end of 2016, due to radiation damage and to increase the readout bandwidth, the original pixel detector was upgraded to a new system, referred to as the CMS Phase-1 pixel detector. As shown in Fig. 7, The original pixel detector is composed of three cylindrical barrel layers and two pairs of endcap disks. It provides three-dimensional position measurements of the hits resulting from the charged particle and has a spatial resolution of about $10 \mu\text{m}$ in the transverse plane and $20\text{-}40 \mu\text{m}$ along the z-axis. The upgraded one has four concentric barrel layers and three disks and provides four-hit coverage up to $|\eta| = 2.5$ with similar spatial resolution as the original one [52]. The strip tracker consists of four subsystems. The Tracker Inner Barrel (TIB) is built from four barrel layers and supplemented by three disks at each end as the Tracker

Inner Disk (TID). Their position measurement resolution is about 13–38 μm . The Tracker Outer Barrel (TOB) and Tracker EndCaps (TEC) are composed of six barrel layers and nine disks respectively, providing position measurements with a resolution of approximately 18-47 μm [51].

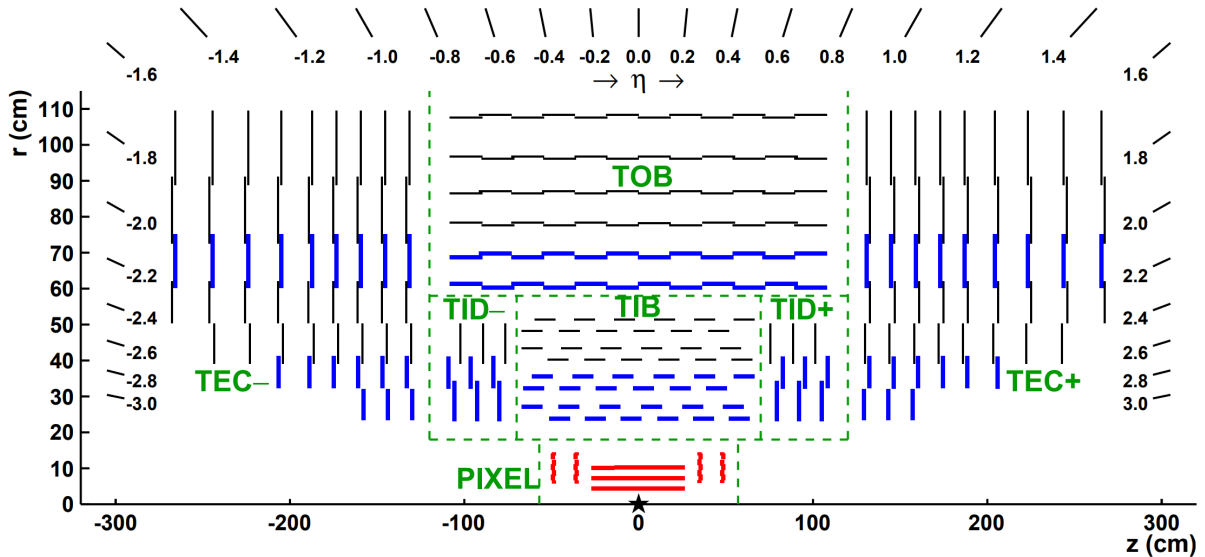


Figure 6: Schematic cross section through the CMS tracker in the r - z plane [51]. Only the upper half of the view symmetric about the horizontal line $r = 0$ is shown here. The center of the tracker is indicated by a star. Green dashed lines group modules to each of the subsystems. The pixel module in the plot is the original one before the Phase-1 upgrade.

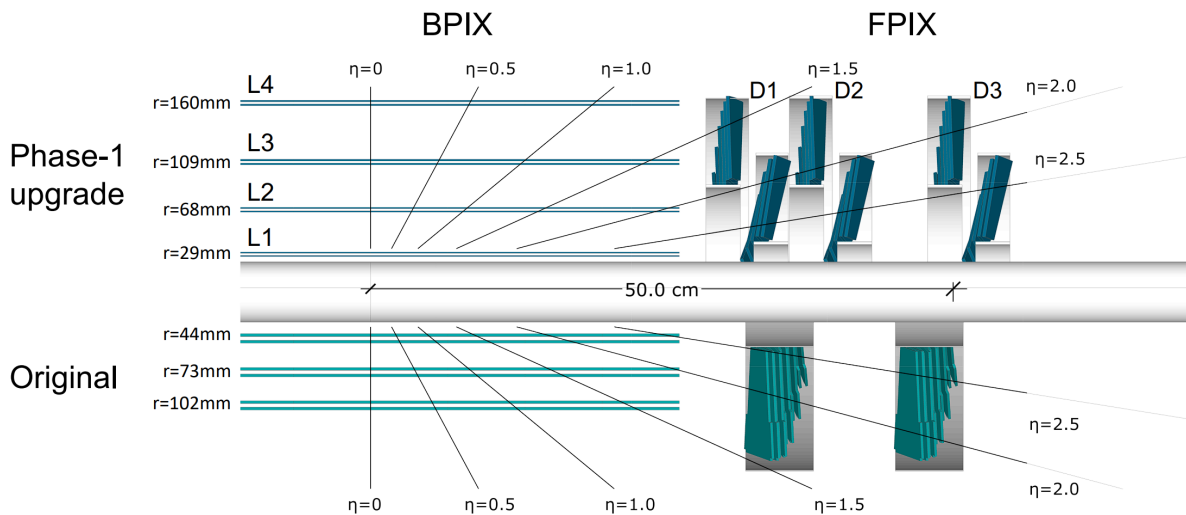


Figure 7: Layout of the CMS Phase-1 pixel detector compared to the original detector layout, in longitudinal view [52]. The BPIX and FPIX are short for barrel and forward disk pixel detectors, respectively.

2.5 Calorimeter

The CMS electromagnetic calorimeter is a homogeneous calorimeter made of transparent lead tungstate (PbWO_4) crystals and has a barrel and two endcap sections. It has a cover-

age of $|\eta| < 3$. A preshower sector is installed in front of each endcap to provide better spatial precision for the forward region [53]. The ECAL measures the energy deposit of electrons and photons and stops them completely. When energetic electrons and photons pass through the crystal, they induce electromagnetic showers, cascades of electrons and photons, and cause scintillation lights proportional to the energy, which are collected by photodetectors at the back of the crystals [4].

The CMS hadronic calorimeter measures the energy of hadrons that produce hadronic showers through the inelastic hadronic interaction with the absorber materials. The HCAL is a sampling calorimeter made by alternating brass or steel absorbers and plastic scintillators. It sits behind the ECAL as seen from the interaction point. The HCAL barrel between the ECAL and the magnet coil is radially restricted and not sufficient to fully absorb the hadronic shower. Thus, a complementing outer hadron calorimeter is placed outside the solenoid. The barrel and endcaps together provide coverage of $|\eta| < 3$. Beyond that, the forward hadron calorimeter (HF) extends the coverage to $|\eta| < 5.2$ and provides luminosity measurements together with other dedicated subdetectors such as the Pixel Luminosity Telescope and the Fast Beam Conditions Monitor [4, 54, 55].

2.6 Muon system

The outer part of the CMS detector is the muon system. It provides muon identification, momentum measurement, and triggering [56–59]. The high-field solenoidal magnet and the flux-return yoke also optimize the muon momentum resolution and trigger capability. Depending on the conditions and needs, the muon system uses three types of gaseous detectors for the cylindrical barrel and planar endcap regions as shown in Fig. 8. Drift tube (DT) chambers with standard rectangular drift cells are used in the barrel region where the rate of muons and neutron-induced background is relatively low and the magnetic field is uniform and mostly contained in the steel yoke. In the endcap regions where the rate of muons and background is high and the magnetic field is large and non-uniform, cathode strip chambers (CSCs) with fast response time and fine segmentation are used. Both DTs and CSCs are organized into 4 stations and together they provide coverage of $|\eta| < 2.4$. The spatial resolution of the DTs is about 250-300 μm in the transverse plane and about 250-600 μm along the z -axis. The spatial resolution of the CSCs is about 48-147 μm [58]. A complimentary, dedicated trigger system consisting of resistive plate chambers (RPCs) is added in both the barrel and endcap regions covering the range $|\eta| < 1.9$. It operates in the avalanche mode and provides timing information for the muon trigger. Although RPCs have coarser position resolution than the DTs or CSCs, they can help to resolve ambiguities in attempting to make tracks from multiple hits in a chamber.

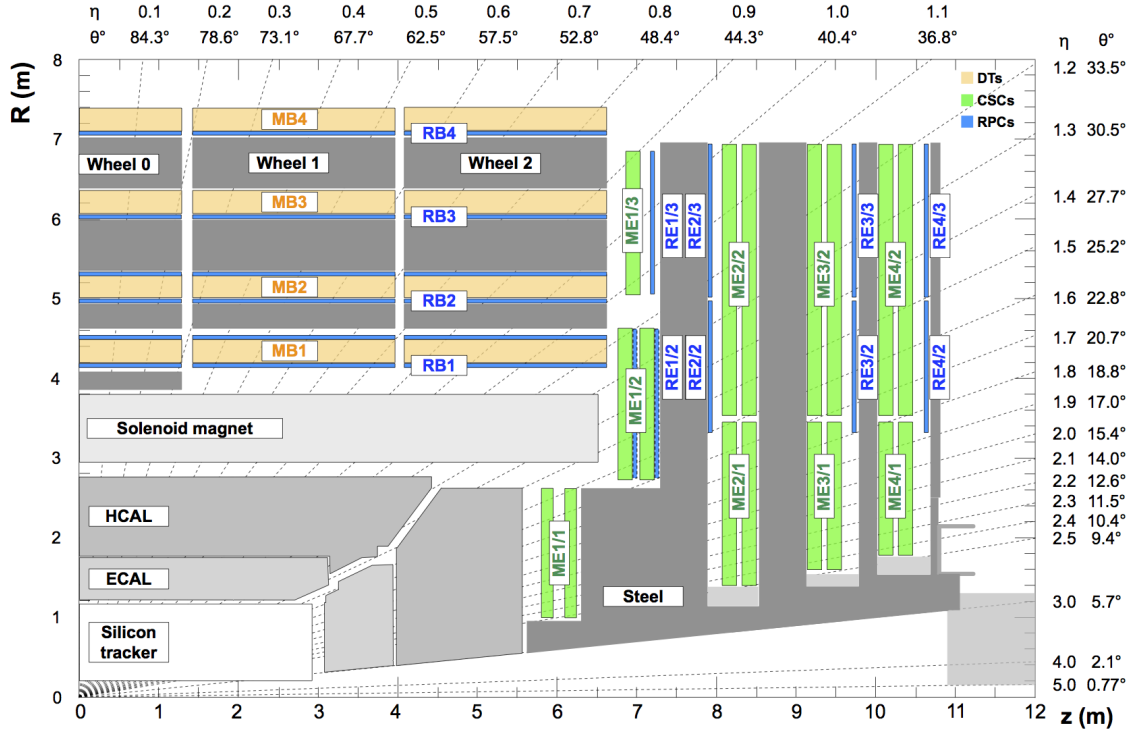


Figure 8: An r - z cross section of a quadrant of the CMS detector with the axis parallel to the beam (z) running horizontally and the radius (r) increasing upward. The interaction point is at the lower left corner. The drift tube stations (DTs) in the barrel (orange), the cathode strip chambers (CSCs) in the endcap (green), and the resistive plate chambers (RPCs) mounted in both the barrel and endcaps (blue) are shown [58].

2.7 Readout system

The LHC provides proton-proton collision at a rate of 40 MHz. It would be impossible to store and process such a huge amount of data, and only a small fraction of these collisions contain events of interest to the CMS physics program. Thus, CMS uses a two-tiered trigger system to select interesting events [4].

The Level-1 trigger (L1) consists of custom hardware with specialized electronics and uses information from the calorimeters and muon detectors to select events at a rate of around 100 kHz within a fixed latency of about $4 \mu\text{s}$ [60]. The second level, known as the high-level trigger (HLT), consists of a farm of processors running a version of the full event reconstruction software optimized for fast processing, and reduces the event rate to around 1 kHz before data storage [61] with detailed and sophisticated selections named HLT paths, which are sets of predefined algorithmic processing steps. Prescale factors may apply for the trigger path with loose cuts to avoid saturating the data-taking bandwidth. The recorded data for each event corresponding to each beam crossing are collected consecutively as blocks called runs. On top of collecting collision data, the trigger and data acquisition systems also record information for detector monitoring, which is used for runs validation [61, 62].

3 Datasets and simulated samples

The data used for this analysis were collected by CMS through the years 2016-2018 and are compared to simulated Monte Carlo (MC) signal and background samples. The full sample collected corresponds to an integrated luminosity of 138 fb^{-1} [55, 63, 64]. The data sets as well as the JSON files labeling the validated runs are summarized in processed Table 1. This analysis uses the unrescaled single muon trigger path `HLT_IsoTkMu24` or `HLT_IsoMu24` for 2016, `HLT_IsoMu27` for 2017 and `HLT_IsoMu24` for 2018, which record events with at least one isolated muon candidate passing the corresponding p_T cut.

Table 1: JSON files and data set names and corresponding integrated luminosities. The letter after the year marks the sub-dataset for that year.

Year	JSON/data file	$\mathcal{L} (\text{fb}^{-1})$
2016	Cert_271036-284044_13TeV_Legacy2016_Collisions16_JSON_MuonPhys.txt /SingleMuon/Run2016*_UL2016_MiniAODv2-v2/MINIAOD	36.31
2017	Cert_294927-306462_13TeV_UL2017_Collisions17_MuonJSON.txt /SingleMuon/Run2017[B,C,D,E,F]-UL2017_MiniAODv2-v1/MINIAOD	41.53
2018	Cert_314472-325175_13TeV_Legacy2018_Collisions18_JSON_MuonPhys.txt /SingleMuon/Run2018[A,B,C,D]-UL2018_MiniAODv2-v[2,3]/MINIAOD	59.74

* includes B-ver1_HIPM, B-ver2_HIPM, C-HIPM, D-HIPM, E-HIPM, F-HIPM, F, G, H.

Processes having four prompt, charged leptons in the final state decayed from one or two electroweak gauge bosons produced in pp collision are simulated at next-to-leading order (NLO) in QCD including all lepton flavors using the `Powheg v2` [65–69] MC event generator. The invariant mass of any two leptons is required to be greater than 4 GeV. The signal channel $pp \rightarrow Z \rightarrow \tau^+ \tau^- \mu^+ \mu^-$ and reference channel $pp \rightarrow Z \rightarrow \mu^+ \mu^- \mu^+ \mu^-$ are isolated from this `Powheg` sample using truth information. Another `Powheg` sample with the invariant mass of lepton pairs greater than 1 GeV is used for cross check.

Other processes leading to a similar final state are grouped into four background categories and modeled with MC simulation. Combinations of prompt and non-prompt charged leptons coming from top quark-antiquark ($t\bar{t}$) and double vector boson (VV) production contribute to the background. The former process and WW and ZZ production with exclusive leptonic decays are simulated at NLO using `Powheg v2` [68–70]. All other VV processes are generated at NLO with the `MadGraph5_aMC@NLO v2.6.5` event generator. Triple vector boson (VVV) production and $t\bar{t}$ production in association with a Z boson ($t\bar{t}+V$) are simulated at leading-order (LO) with `MadGraph5_aMC@NLO v2.6.5` [71]. Higgs (H) boson production and subsequent decay into four charged leptons is simulated with `Powheg v2` [72, 73] and `JHUGEN v.7.0.11` [74–76]. A full list of MC samples and their cross sections is shown in Table 2. The cross sections are taken from Ref. [77].

All processes are simulated using the NNPDF3.1 parton distribution functions (PDFs) at next-to-next-to-leading order (NNLO) [78]. The initial and final state radiation of gluons

and photons cause corrections to the event generation. These higher-order corrections can be included in the hard process calculation or modeled as parton shower generating secondary partons [79]. The parton shower and subsequent hadronization are simulated with `Pythia 8` [80, 81]. If higher-order corrections are considered at the hard scattering level, both the perturbative matrix element calculation and the parton shower can describe the same process, and matching algorithms are used to avoid double counting. The underlying events coming from the beam-beam remnants and the particles that arise from multiple-parton interactions are modeled using the CP5 tune [79, 82]. Additional inelastic pp interactions in the same or adjacent bunch crossings are simulated for all processes and events are reweighted to match the measured number of pileup interactions in the data. The detector response including the trigger path is simulated using `GEANT4` [83]. The same physics objects and event reconstruction, as explained in the next chapter, are subsequently applied to collision data and simulation. The Run 2016 is split into two different reconstruction versions using different track reconstructions, the “pre-VFP” era and the “post-VFP” era. They are simulated separately.

Table 2: Simulation samples and cross sections.

Samples	σ (pb)
ZZTo4L_TuneCP5_13TeV_powheg_pythia8	1.26
ZZTo4L_M-1toInf_TuneCP5_13TeV_powheg_pythia8	13.74
TTToSemiLeptonic_TuneCP5_13TeV_powheg_pythia8	364.31
TTTo2L2Nu_TuneCP5_13TeV_powheg_pythia8	87.31
TTZToLLNuNu_M-10_TuneCP5_13TeV-amcatnlo-pythia8	0.253
WWTo2L2Nu_TuneCP5_13TeV_powheg-pythia8	12.18
WZTo2Q2L_mllmin4p0_TuneCP5_13TeV-amcatnloFXFX-pythia8	5.60
WZTo3LNU_TuneCP5_13TeV-amcatnloFXFX-pythia8	4.43
ZZTo2Q2L_mllmin4p0_TuneCP5_13TeV-amcatnloFXFX-pythia8	3.22
ZZTo2L2Nu_TuneCP5_13TeV_powheg-pythia8	0.56
WWZJetsTo4L2Nu_4F_TuneCP5_13TeV-amcatnlo-pythia8	6.02×10^{-4}
WZZ_TuneCP5_13TeV-amcatnlo-pythia8	5.56×10^{-2}
ZZZ_TuneCP5_13TeV-amcatnlo-pythia8	1.40×10^{-2}
ZZGTo4L_TuneCP5_4f_NLO_13TeV-amcatnlo-pythia8	2.20×10^{-2}
GluGluHToZZTo4L_M125_TuneCP5_13TeV_powheg2_JHUGenV7011_pythia8	1.21×10^{-2}
VBF_HToZZTo4L_M125_TuneCP5_13TeV_powheg2_JHUGenV7011_pythia8	1.03×10^{-3}

4 Event reconstruction

4.1 Particle Flow

CMS uses the particle-flow (PF) algorithm to reconstruct the physics objects and collision events with the information from various subdetectors. The reconstruction starts by building three main PF elements: the inner tracks of charged particles in the tracker, the muon tracks in the muon detectors, and the clusters of energy deposits in the calorimeter, and then reconstructs and identifies vertices and particles by connecting the PF elements from different subdetectors with a link algorithm. As shown in Fig. 9, the particles are reconstructed in the order of muons, electrons, charged hadrons, neutral hadrons, and photons and then used to reconstruct jets and missing transverse energy. The details of the PF reconstruction are in Ref. [84].

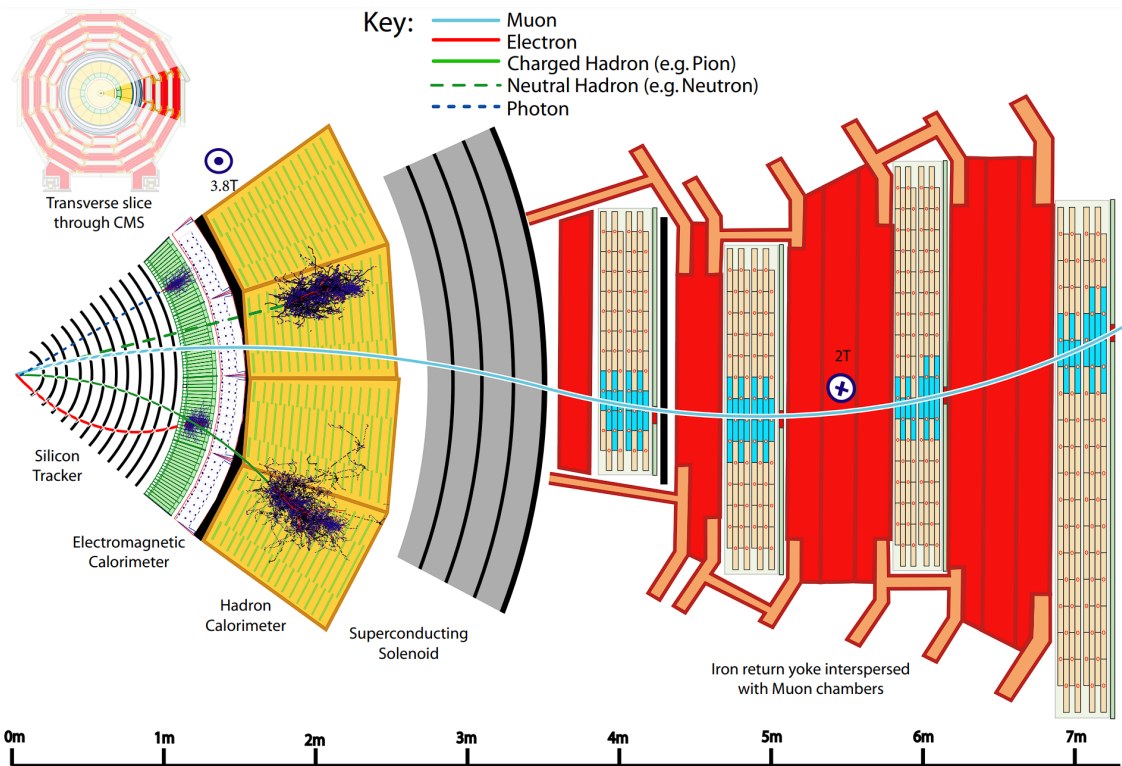


Figure 9: Schematic view of a transverse slice of the CMS detector from the beam interaction region to the muon detector [84].

The inner track reconstruction is based on Kalman filtering. It starts with seed generation with few hits compatible with a charged-particle trajectory and builds tracks with pattern recognition. After resolving ambiguity by comparing the shared hits and χ^2 value of different tracks, it performs a final fit to determine the properties of the tracks such as its origin, p_T , and impact parameters and discards tracks that fail certain specified criteria [51, 85].

The *standalone-muon tracks* are built by using a Kalman-filter technique exploiting infor-

mation from the muon system and used as input for muon track reconstruction together with the inner tracks reconstructed independently with hits in the tracker. The *tracker muon tracks* are built by inner tracks with p_T larger than 0.5 GeV and total momentum p larger than 2.5 GeV extrapolated to the muon system and matched with at least one muon segment in the DT or CSC. The *global muon tracks* are built by matching *standalone-muon tracks* with inner tracks requiring that the parameters of the two tracks propagated onto a common surface are compatible. About 99% of the muons produced within the geometrical acceptance of the muon system are reconstructed either as a *tracker muon track* or as a *global muon track*, and very often as both, because of the high efficiency of the tracker and the muon system. Global and tracker muons sharing the same tracker track are merged into a single candidate. The muon tracks are refitted after matching with all the hits to give the best tracks. The muon momentum resolution is 1-3% for muons with momenta up to approximately 100 GeV and around 6% for $p_T < 1$ TeV. The details of muon tracks reconstruction are in Ref. [57, 58].

The energy clusters in the calorimeter are built with seeds identified as cells with an energy larger than a given seed threshold and the energy of the neighboring cells. Starting with seeds, topological clusters are formed by adding cells that share a corner with a cell already in the cluster and have an energy greater than twice the noise level. The clusters are then reconstructed within topological clusters with an expectation-maximization algorithm based on a Gaussian-mixture model [84].

4.2 Primary vertex

For vertices reconstruction, tracks consistent with being produced promptly in the primary interaction region are selected, by checking the significance of the transverse impact parameter relative to the center of the beam spot, the number of hits, and the normalized χ^2 from the track fit. The selected tracks are clustered as candidate vertices using a deterministic annealing algorithm [86] based on their z -coordinates of the points of closest approach to the center of the beam spot. The candidates with at least two tracks are fitted using an adaptive vertex fitter [87] to compute the best estimate of vertex parameters, including its x , y , z position, the covariance matrix, and the performance of the fit. The fit assigns each track i in the vertex a weight ω_i between 0 and 1 reflecting the likelihood that it genuinely belongs to the vertex. Tracks that are more consistent with the position of the reconstructed vertex have weights closer to 1 and vice versa. The number of degrees of freedom in the fit is calculated by summing the weight of all tracks associated with the vertex as

$$n_{\text{d.o.f.}} = -3 + 2 \sum_{i=1}^{\text{\#tracks}} \omega_i. \quad (4.1)$$

The $n_{\text{d.o.f.}}$ is therefore strongly correlated with the number of tracks compatible with arising from the interaction region. The primary vertex (PV) is taken to be the vertex corresponding to the hardest scattering in the event, evaluated using tracking information

alone, as described in Section 9.4.1 of Ref. [88]. A detailed description of the vertex reconstruction in CMS is in Ref. [51].

4.3 Muon identification

Different muon identification (ID) criteria are defined as groups of variables of muon tracks to enable each analysis to adjust the balance between selection efficiency and purity as desired [58]. The identification types used in this analysis are the `loose` muon ID and `tight` muon ID.

The `loose` muon ID requires the muon selected by the PF algorithm to be reconstructed as either a tracker or a global muon. It aims to identify prompt muons originating at the primary vertex, and muons from light and heavy flavor decays, as well as maintain a low rate of the misidentification of charged hadrons as muons.

The `tight` muon ID aims to further suppress muons from decay in flight and from misidentified hadrons punching through the HCAL as well as cosmic muons. A `tight` muon is a `loose` muon with an inner track that uses hits from at least six layers of the inner tracker including at least one pixel hit, and it must be reconstructed as both a tracker muon having segment matching in at least two of the muon stations and a global muon. The global muon fit must have $\chi^2/\text{d.o.f.} < 10$ and include at least one hit from the muon system. A `tight` muon must have a transverse impact parameter $|d_{xy, \text{PV}}| < 0.2$ cm and a longitudinal impact parameter $|d_{z, \text{PV}}| < 0.5$ cm relative to the primary vertex to be compatible with it.

5 Event selections

The selected event needs to have a primary vertex with its number of degrees of freedom $n_{\text{d.o.f.}} > 4$, transverse distance with respect to the beam pipe $|d_{\text{vtx},xy}| < 2$ cm and longitudinal distance from the interaction point along the beam pipe $|z_{\text{vtx}}| < 24$ cm.

For the baseline muon selection, a reconstructed muon candidate must satisfy the kinematic requirements $p_{\text{T}} > 2.5$ GeV and $|\eta| < 2.4$, and the impact parameter requirements $|d_{xy}| < 0.5$ cm, $|d_z| < 1$ cm, and $\text{SIP}_{3\text{D}} < 4$ with respect to the primary vertex. The $\text{SIP}_{3\text{D}}$ is the significance of the impact parameter defined as the impact parameter to the PV divided by its uncertainty:

$$\text{SIP}_{3\text{D}} = \frac{d_{xyz}}{\sigma_{d_{xyz}}}. \quad (5.1)$$

The impact parameter is defined by its best track for a muon candidate.

To suppress the muon candidates from weak decays within jets, the muon isolation variable is evaluated relative to its p_{T} by summing up the energy of other PF candidates such as hadrons and photons within a geometrical cone of radius $\Delta R = \sqrt{(\Delta\phi)^2 + (\Delta\eta)^2} = 0.4$ surrounding the muon [58]. The PF-based muon relative isolation is defined as:

$$\text{RelPFIso} = \frac{\sum^{\text{charged hadrons}} p_{\text{T}} + \max\left(\sum^{\text{neutral hadrons}} E_{\text{T}} + \sum^{\text{photons}} E_{\text{T}} - \Delta\beta, 0\right)}{p_{\text{T}}^{\mu}}, \quad (5.2)$$

where $\Delta\beta = \frac{1}{2} \sum_{\text{PU}}^{\text{charged hadron}} p_{\text{T}}$ is the correction for charged hadron deposits associated with pileup vertices.

The analysis requires exactly four muons in an event, which have to pass different ID and isolation criteria. The muon selected leading in p_{T} must pass the `tight` muon ID and the `tight` PF-isolation working point, i.e. $\text{RelPFIso} < 0.15$. Exactly three additional muons must pass the `loose` muon ID, be reconstructed as both a tracker and a global muon, and pass the `loose` PF-isolation working point, i.e. $\text{RelPFIso} < 0.25$. The `tight` and `loose` isolation working points are defined to achieve efficiencies of 95% and 98%, respectively [58]. The sum of charges of the four selected muons must be 0. For the `ZZTo4L` sample, we require the reconstructed muons to be matched with truth-level muons having the same charge with the distance $\Delta R(\mu_{\text{reco}}, \mu_{\text{truth}}) < 0.1$. Finally, any pair of muons is required to be separated by $\Delta R > 0.02$ to avoid overlap and suppress contribution from split tracks.

The transverse momenta of the three leading selected muons are furthermore required to satisfy $p_{\text{T}} > 26, 3.5, 3.5$ GeV. For 2017, the leading muon must have a transverse momentum $p_{\text{T}} > 29$ GeV. The fourth muon is required to have $p_{\text{T}} > 3.5$ GeV in case its $|\eta| < 1.2$ and 2.5 GeV otherwise. Additionally, the leading muon is also required to match with one of the trigger objects with $\Delta R < 0.3$.

All opposite-sign (OS) muon pairs are required to have an invariant mass greater than 4 GeV. The four muons are grouped into two opposite-charge pairs. The pair with higher invariant mass is denoted as “ Z_1 ”, and the pairs maximizing m_{Z_1} are chosen. The high-mass dimuon pair is required to be within $12 < m_{Z_1} < 75$ GeV in order to suppress contamination from $Z \rightarrow \mu\mu$ decays and lower-mass dimuon resonances. The tracks of these four muons are further required to form a valid vertex with the Kalman vertex fitting [89]. The four muon invariant mass distribution is examined in the 40-100 GeV window.

6 Background estimation

The dominant background in this measurement comes from $ZZ^{(*)} \rightarrow 4\mu$ events, where all four muons are produced promptly via the Z decay. Small additional contributions come from $t\bar{t}(+V)$, VV , VVV , and H production. These backgrounds are modeled using MC simulation, corrected by several muon-related data-to-MC scale factors, which are detailed in the next chapter. The background from non-prompt muons is estimated with a data-driven technique explained here.

The shape and normalization of the background due to non-prompt muons, mostly from QCD and pile-up, is estimated using the ABCD method as shown in Fig. 10 (a). The selection of the previous chapter defines the signal region (A). The control regions B, C, and D are defined by inverting the charge condition on the four muons and/or the isolation cut on the three non-leading muons while keeping all other selections unchanged. In the signal region, the four muons in an event must have an equal number of opposite-sign (OS) charges. Events in the like-sign (LS) region have a like-sign combination of muons, $\mu^{\pm}\mu^{\pm}\mu^{\pm}\mu^{\mp}$ or $\mu^{\pm}\mu^{\pm}\mu^{\pm}\mu^{\pm}$. Events in the non-isolated region have at least one muon with the relative PF-based isolation $\text{RelPFIsol} > 0.25$. Fig. 11 shows a comparison of distributions of the isolation below 1 without any cut on it for the three non-leading muons between OS and LS data. The remaining contribution of events with any prompt muon has been subtracted from the OS data (points) using MC information. In the LS region, this contribution is negligible and not corrected for. Both the shape and the normalization of the distributions of the relative isolation clearly do not depend on the OS/LS requirement. This enables the use of the ABCD methods, for which two uncorrelated variables must be used to define the four regions. A comparison of distributions of the isolation variables in the non-isolated control region is shown in Fig. 23.

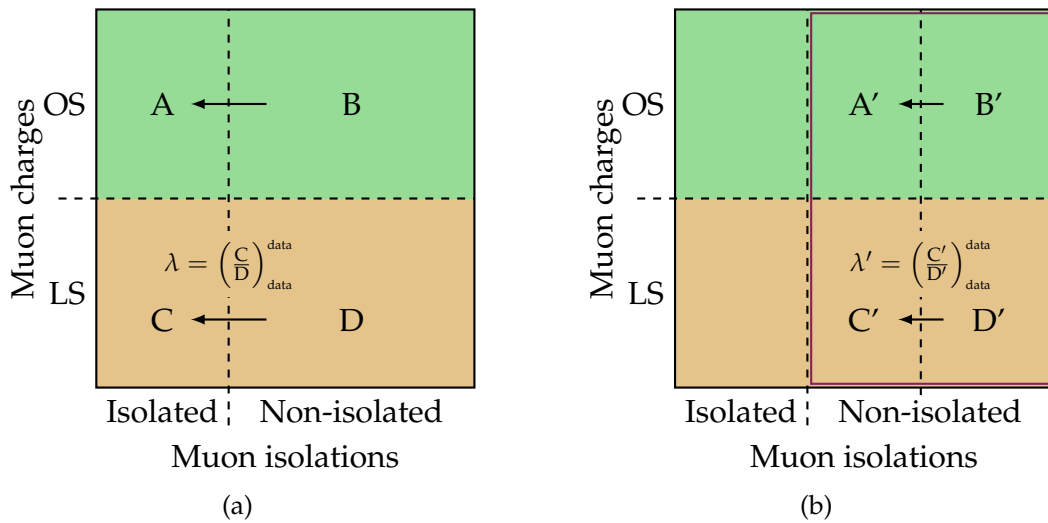


Figure 10: The signal region and control regions for the ABCD method (a). The validation regions for the closure test (b).

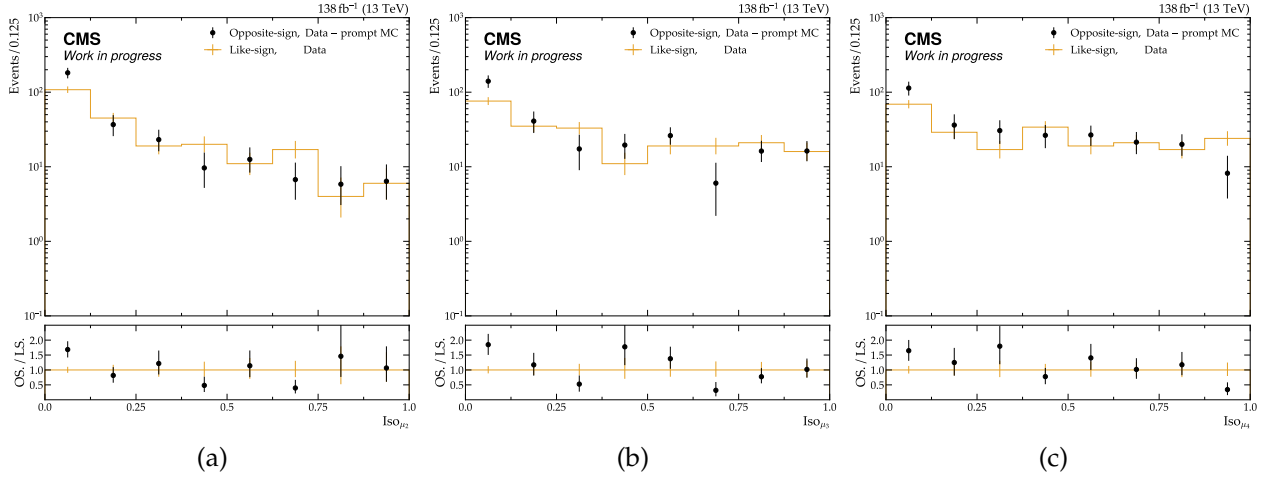


Figure 11: Distributions and statistical uncertainties of isolation variables of the three muons with lower p_T in the opposite-sign and like-sign region.

A transfer factor λ is measured in the two LS control regions, C and D, as the ratio of the (integrated) number of events in data in each region: $\lambda = N_{\text{data}}^C / N_{\text{data}}^D$. This transfer factor is then applied to MC-truth-subtracted data in region B in order to predict the non-prompt background in the signal region A,

$$N_{\text{non-prompt}}^A = N_{\text{data-MC}_{\text{prompt}}}^B \cdot \lambda. \quad (6.1)$$

The relevant yields in the four regions are shown in Table 3. The resulting extrapolation factor is found to be

$$\lambda = 0.156 \pm 0.035, \quad (6.2)$$

where the uncertainty is due to the limited number of events in regions C and D. The uncertainty in λ is assigned as a systematic uncertainty of the non-prompt background estimation in the final maximum likelihood fit to the data. The bin-by-bin statistical uncertainties in each bin of the LS prediction for region A are obtained from the corresponding ones in region B, scaled by λ .

Table 3: The selection criteria and yield in each region. The uncertainty in regions C and D is obtained from the quadratic sum of the bin-by-bin statistical uncertainties in the data. The uncertainty in B is the bin-by-bin uncertainty of the MC-subtracted data obtained from Gaussian error propagation in each bin, while the uncertainty in region A additionally contains the uncertainty in λ .

Charge combination	Isolation cut	Region	Yield
Opposite-sign	Isolated	A	$N_{\text{extrapolated}} = 29.9_{-7.5}^{+7.6}$
Opposite-sign	Non-isolated	B	$N_{\text{data-MC}_{\text{prompt}}} = 191.5_{-22.3}^{+23.3}$
Like-sign	Isolated	C	$N_{\text{data}} = 31.0_{-5.5}^{+6.6}$
Like-sign	Non-isolated	D	$N_{\text{data}} = 199.0_{-14.1}^{+15.1}$

The closure of the estimation is tested using validation regions divided from regions B and D as shown in Fig. 10 (b) with varied isolation requirements. The OS and LS region follow the definition above. The three non-leading muons in the events in regions A' and C' have the relative isolation $\text{RelPFIso} < 0.4$ and at least one of them has $\text{RelPFIso} > 0.25$. Events in the regions B' and D' have at least one muon with the relative isolation $\text{RelPFIso} > 0.4$. Again, in the OS region, the remaining contribution of events with any prompt muon has been subtracted from the OS data using MC information. Another transfer factor for the validation test λ' is measured in the regions C' and D' as the ratio of the (integrated) number of events in data in each region: $\lambda' = N_{\text{data}}^{C'}/N_{\text{data}}^{D'}$. This transfer factor is then applied to MC-truth-subtracted data in region B' in order to predict the non-prompt background in region A' as

$$N_{\text{extrapolated}}^{A'} = N_{\text{data-MC}_{\text{prompt}}}^{B'} \cdot \lambda'. \quad (6.3)$$

which is then compared with the actual number of events in region A', $N^{A'}$.

The yields in the four validation regions and the prediction are shown in Table 4. The resulting extrapolation factor is found to be $\lambda' = 0.150 \pm 0.037$, where the uncertainty is due to the limited number of events in regions C' and D'. The differences between the actual yield and prediction in region A',

$$N_{\text{data-MC}_{\text{prompt}}}^{A'} - N_{\text{extrapolated}}^{A'} = 20.5_{-14.9}^{+15.9}, \quad (6.4)$$

is consistent with 0 within 1.41 times its uncertainty.

Table 4: The selection criteria and yield in each validation region. The uncertainties are calculated w the same way described in Table 3.

Charge combination	Isolation cut	Region	Yield
Opposite-sign	[0.25, 0.4]	A'	$N_{\text{data-MC}_{\text{prompt}}} = 42.8_{-13.1}^{+14.2}$
			$N_{\text{extrapolated}} = 22.3_{-6.1}^{+6.2}$
Opposite-sign	[0.4, 1.0]	B'	$N_{\text{data-MC}_{\text{prompt}}} = 148.7_{-18.0}^{+19.0}$
Like-sign	[0.25, 0.4]	C'	$N_{\text{data}} = 26.0_{-5.1}^{+6.1}$
Like-sign	[0.4, 1.0]	D'	$N_{\text{data}} = 173.0_{-13.1}^{+14.2}$

7 Systematics

7.1 Corrections to simulated samples

The differences in reconstruction and selection efficiencies between the simulation and data are corrected by several muon-related data-to-MC scale factors (SFs), which are detailed in the following subsections. The central scale factors provided by the CMS Muon Physics Object Group (Muon POG) [90] are used if available.

7.1.1 L1 pre-firing

The L1 pre-firing event weights provided by the CMS Physics Performance & Datasets group are applied to account for the loss of trigger efficiency due to the incorrect assignment of the muons to the LHC bunch crossings in the L1 trigger for 2016 and 2017 respectively. This effect is negligible in 2018 and there is no pre-firing weight for 2018.

7.1.2 Tracker muon reconstruction

The track reconstruction scale factors provided by the Muon POG are applied to account for differences in the efficiency of reconstructing a tracker muon from a track between data and MC to all muons for each year respectively.

7.1.3 Global muon reconstruction

There are no central scale factors to correct for the global muon reconstruction efficiency differences between data and MC. It was recommended by the Muon POG to compute the ratio of the number of events passing the entire event selection including the requirement of the muons to be global (numerator) and the number of events passing the entire event selection without requiring muons to be global (denominator). Using the ZZ4L samples and data for different years, the ratios are calculated within the four muon invariant mass window $[80, 100]$ GeV where the purity of prompt muons from the $Z \rightarrow \mu^+ \mu^- \mu^+ \mu^-$ process is very high. The SFs are obtained by comparing the efficiency ratios between data and MC as in Table 5 and applied to correct for these differences. The uncertainties in the table are statistical.

Table 5: Global muon ID scale factors

Year	scale factors
2016 preVFP	0.996 ± 0.034
2016 postVFP	1.046 ± 0.027
2017	1.004 ± 0.022
2018	0.991 ± 0.020

7.1.4 Muon ID

The analysis uses two different ID working points: the `tight` ID for the muon leading in p_T and the `loose` ID for the other three. For both IDs, the centrally provided SFs are used to correct for differences between data and MC.

7.1.5 Muon isolation

The leading muon is required to pass the `tight` relative PF-based isolation working point on top of the `tight` ID. The other three muons are required to pass the `loose` relative PF-based isolation working point on top of the `loose` ID working point. The corresponding centrally provided SFs are used.

7.1.6 Muon trigger efficiency

The leading muon is required to pass the `tight` ID and `tight` isolation working points and to have $p_T > 26 \text{ GeV}$ (29 GeV for 2017), which ensures operation in the plateau of efficiency of the single isolated muon trigger. The leading muon is also required to match with one of the trigger objects with $\Delta R < 0.3$. The trigger SF provided by the POG is applied to correct for differences in the trigger efficiency between data and MC.

7.1.7 Muon momentum scale and resolution

The “Rochester correction” is applied for the muon momentum scale and resolution provided by the Muon POG to the data and MC samples respectively [91, 92]. The correction is applied before any p_T cut.

7.2 Systematic uncertainties

Several systematic uncertainties are considered in the final binned maximum-likelihood template fit described in chapter 8 to the data in the distribution of the invariant mass of the four muons. These can affect the shape of that distribution, its normalization, or both. A list of uncertainties considered is given in table 6. The shape variations brought by each systematics are shown in sec A.2 for the signal and reference channel. All uncertainties in data-to-MC scale factors are taken into account by shifting the respective scale factor within its uncertainty and creating varied histogram templates for the final fit. The statistical and systematic uncertainties of muon-related scale factors are separated. According to the MUO POG, the systematic uncertainties on these scale factor measurements are correlated among data-taking periods while the statistical uncertainties are uncorrelated among the different years. The luminosity uncertainty is taken into account following the recommendation of the CMS Luminosity POG [93], while for the cross section uncertainties, the following pre-fit values are used [77]:

- $t\bar{t}(+V)$: 5% [94, 95]
- VV : 20% [96]
- VVV : 25% [97]
- H : 10% [98]

The correlation of the luminosity uncertainty among the data-taking years is implemented according to Ref. [93], the cross section uncertainties affect only the respective process and are fully correlated among years. The muon-related uncertainties, which affect both the shape and normalization of the distribution, are uncorrelated among years but fully correlated between all simulated processes in a given year.

7.2.1 Data-driven estimation of non-prompt backgrounds

The uncertainty in the normalization of the data-driven prediction of the non-prompt background in the SR is obtained by shifting the predicted shape up and down within the uncertainty in λ . This corresponds to a relative yield uncertainty of $\pm 22.4\%$. This number is smaller than that derived from table 3 because the latter additionally included bin-by-bin statistical uncertainties, which are taken into account separately in the final fit. In addition to this normalization-only uncertainty, other systematic uncertainties can affect this data-driven prediction through the subtraction of MC in region B. In order to take these effects into account, the extrapolation from B to A is repeated with the nominal λ using the varied MC-subtracted from data in region B. As a consequence, all systematic uncertainties that affect simulation with four prompt muons in region B also affect the data-driven prediction of the non-prompt background in region A. However, the effect of any systematic uncertainty is much smaller than the uncertainty in the extrapolation factor λ itself.

7.2.2 QCD factorization and renormalization scales

Uncertainties from the QCD factorization and renormalization scales, μ_R and μ_F , are estimated respectively using the procedure recommended by Ref. [99]. The nominal scales are $\mu_R = \mu_F = 1$. Each simulated sample is reweighted with the weights corresponding to μ_R and μ_F varied independently by 1/2 and by 2 while the other being 1. Each varied distribution is normalized to the nominal distribution before any cuts. As shown in Fig. 25 in the Appendix, these four cases are the dominant variations and they have a crossing in the $Z \rightarrow 4\mu$ process. The varied histograms are used as the uncertainty templates for the fit.

7.2.3 PDF+ α_s sets

The uncertainty in the choice of PDF sets is estimated by reweighting each simulated sample using the procedure recommended by Ref. [99], with the error sets being $N = 100$

eigenvectors of NNPDF 3.1. For each sample's distribution, the PDF uncertainty for a given bin content b is obtained as

$$\delta_b^{\text{PDF}} = \sqrt{\sum_{i=1}^N (b_i - b_0)^2}, \quad (7.1)$$

where i is the index of each PDF choice, and b_i and b_0 are the bin contents obtained by using the varied and nominal weight, respectively. For the sample with a PDF set having α_s variations, the PDF+ α_s uncertainty is calculated as

$$\delta_b^{\alpha_s} = \frac{b(\alpha_s = 0.1195) - b(\alpha_s = 0.1165)}{2}, \quad \delta_b^{\text{PDF}+\alpha_s} = \sqrt{(\delta_b^{\text{PDF}})^2 + (\delta_b^{\alpha_s})^2}, \quad (7.2)$$

where $b(\alpha_s = 0.1195)$ and $b(\alpha_s = 0.1165)$ are the bin contents obtained by using the varied weight corresponding to different α_s values. Equations (7.1) and (7.2) are adapted from Eq. (20),(27),(28) of Ref. [100], which give the combined PDF+ α_s uncertainty for any bin of a differential distribution evaluated using Hessian PDF sets. The uncertainties per bin are taken to be fully correlated, and two varied histogram templates are created for the final fit with each bin shifting up and down within its uncertainties.

Table 6: Systematic uncertainties and their effect on shape/normalization, different processes, and correlations among years and processes. "unc." refers to no correlation between whatever follows. All uncertainties affecting simulated processes with four prompt muons are propagated onto the estimation of the non-prompt background, even if not stated explicitly in this table.

Uncertainty	Shape/norm.	Process(es)	Correlation
Integrated luminosity	norm.	all simulated	among years according to [93]
Cross section top (+V)	norm.	top	fully among years
Cross section VV	norm.	VV	fully among years
Cross section VVV	norm.	VVV	fully among years
Cross section H	norm.	H	fully among years
Muon: global ID SF	norm.	all simulated	unc. years, fully among procs.
Extrapolation factor λ	norm.	non-prompt	single number
L1 pre-firing SF	shape + norm.	in 2016, 2017	unc. years, fully among procs.
Tracker muon reco. SF Stat.	shape + norm.	all simulated	unc. years, fully among procs.
Muon: Loose/Tight ID SF Stat.	shape + norm.	all simulated	unc. years, fully among procs.
Muon: isolation SF Stat.	shape + norm.	all simulated	unc. years, fully among procs.
Muon: trigger SF Stat.	shape + norm.	all simulated	unc. years, fully among procs.
Tracker muon reco. SF Syst.	shape + norm.	all simulated	fully among procs. & years
Muon: Loose/Tight ID SF Syst.	shape + norm.	all simulated	fully among procs. & years
Muon: isolation SF Syst.	shape + norm.	all simulated	fully among procs. & years
Muon: trigger SF Syst.	shape + norm.	all simulated	fully among procs. & years
μ_R variations	shape + norm.	all simulated	fully among years, unc. procs.
μ_F variations	shape + norm.	all simulated	fully among years, unc. procs.
PDF+ α_s variations	shape + norm.	all simulated	fully among years, unc. procs.
Bin-by-bin stat.	norm. per bin	each bin	unc. bins

8 Signal extraction

The yield of $Z \rightarrow \tau^+ \tau^- \mu^+ \mu^- \rightarrow \mu^+ \mu^- \mu^+ \mu^-$ events is extracted from a binned maximum-likelihood template fit of the expected signal and background to the data using the distribution of the invariant mass of the four selected muons with the `Higgs Combine`, a statistical analysis tool developed by the CMS Higgs combination group [101]. The distributions before the fit are shown in Fig. 12 as used in the background-only fit (left) and the signal+background fit (right). The normalized pre-fit distributions are shown in Fig. 13. Each systematic described in the previous chapter is taken into account as a nuisance parameter in this fit. Uncertainties not affecting the shape of the distribution are modeled with lognormal prior distributions with a standard deviation corresponding to the value given in the previous chapter, while those affecting the shape and normalization are modeled with Gaussian priors. The bin-by-bin statistical uncertainties due to the finite sample size are taken into account by one additional nuisance parameter per bin with a Gaussian prior distribution, following the Barlow-Beeston lite method [102, 103].

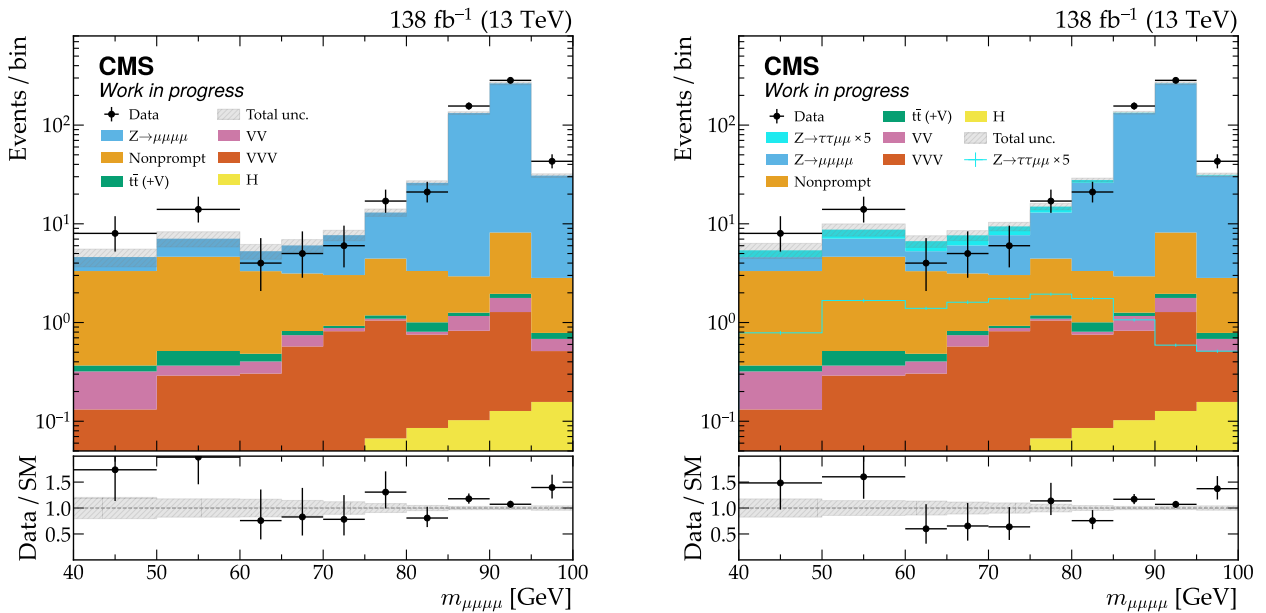


Figure 12: Pre-fit four muon invariant mass distribution without (left) and with (right) the signal sample.

In the background-only fit, no signal contribution is considered and the normalization of the $Z \rightarrow 4\mu$ background, $r_{Z \rightarrow 4\mu}$, is an unconstrained parameter of interest (POI) in the fit. Its yield is determined by $N(Z \rightarrow \mu^+ \mu^- \mu^+ \mu^-) = r_{Z \rightarrow 4\mu} \times N^{\text{SM}}(Z \rightarrow \mu^+ \mu^- \mu^+ \mu^-)$. In the signal+background fit, the ratio r of the $Z \rightarrow \tau^+ \tau^- \mu^+ \mu^-$ process to the $Z \rightarrow 4\mu$ is taken into account as an additional, unconstrained POI. Thus, the normalization of the $Z \rightarrow \tau^+ \tau^- \mu^+ \mu^-$ is determined by the normalization of the $Z \rightarrow 4\mu$ process and the ratio together and the yield by $N(Z \rightarrow \tau^+ \tau^- \mu^+ \mu^-) = r \times r_{Z \rightarrow 4\mu} \times N^{\text{SM}}(Z \rightarrow \tau^+ \tau^- \mu^+ \mu^-)$. The expected number of events is listed in Table 12.

The fit is performed with the `Higgs Combine` tool to maximize the likelihood and ex-

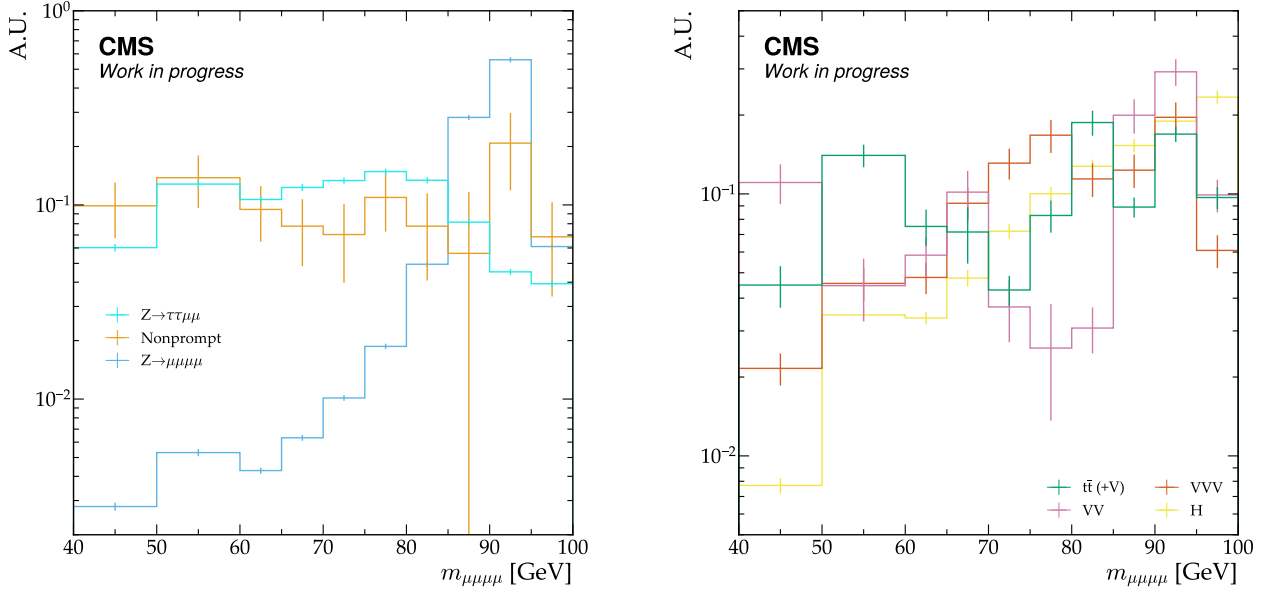


Figure 13: The normalized pre-fit four muon invariant mass distributions. The uncertainty includes statistics and systematics described in the previous section.

tract the parameters of interest as well as the post-fit values and uncertainties of each nuisance parameter. The input to the fit (“pre-fit distribution”), without and with the signal included, is shown in Fig. 12, left and right respectively. Additional pre-fit kinematics distributions with signal included are shown in sec A.4.

8.1 Sensitivity to $Z \rightarrow 4\mu$

Before processing with the signal, the fit performance and reliability are checked by examining the post-fit signal strength of the $Z \rightarrow \mu^+ \mu^- \mu^+ \mu^-$ process, which is the reference channel and present in the same distribution used for the $Z \rightarrow \tau^+ \tau^- \mu^+ \mu^-$ process. Using the fit procedure and inputs described above, the fitted result is $r_{Z \rightarrow 4\mu} = 1.115^{+0.071}_{-0.068}$, which is well compatible with the SM expectation of $r_{Z \rightarrow 4\mu} = 1$. The post-fit distribution of the four-muon invariant mass is shown in Fig. 14 (left), while the profiled negative log-likelihood is shown in Fig. 14 (right). The post-fit nuisance parameter values, uncertainties, and impacts on the fitted signal strength for the $Z \rightarrow \mu^+ \mu^- \mu^+ \mu^-$ process are shown in Fig. 19. It is evident that the post-fit values of all the nuisance parameters agree with their prior distributions. Additional background-only post-fit kinematics distributions are shown in sec A.4.

8.2 Expected signal sensitivity

Before fitting the signal+background model with the real data, a fit of the expected signal and background to the signal+background Asimov dataset is performed in order to validate the constraints imposed on the various nuisance parameters by the fit. The post-fit signal strength r , defined as the signal strength modifier of the the $Z \rightarrow \tau^+ \tau^- \mu^+ \mu^-$

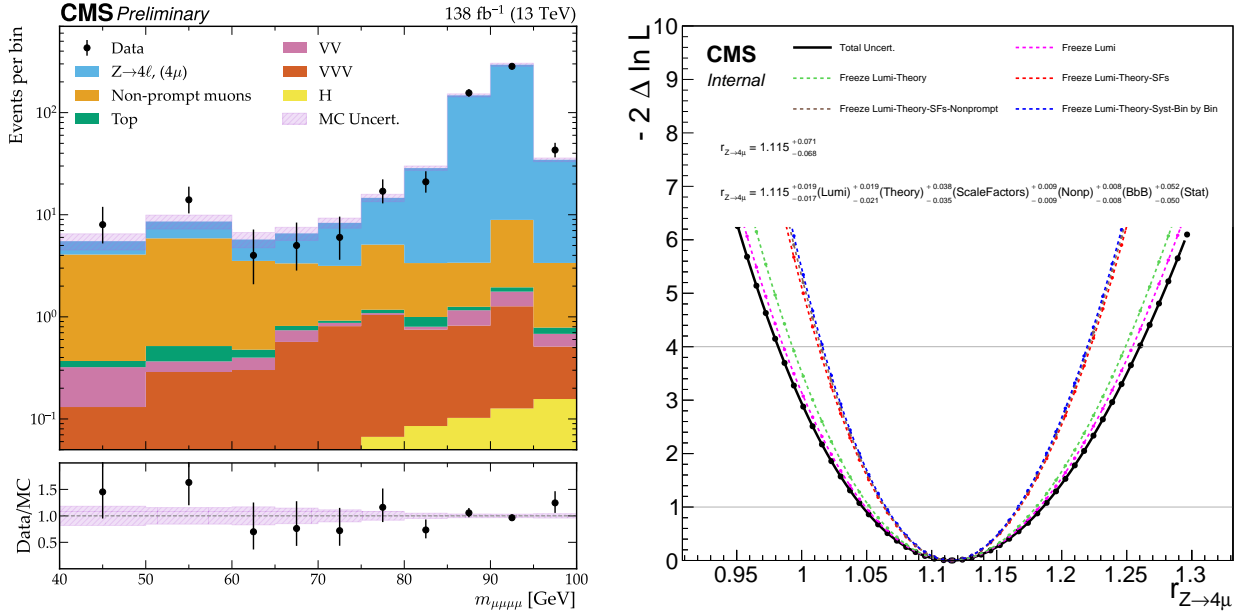


Figure 14: Background-only fit result for the $Z \rightarrow \mu^+ \mu^- \mu^+ \mu^-$ process.

process relative to that of the $Z \rightarrow 4\mu$, is $r^{\text{SM}} = 1.0^{+4.348}_{-4.098}$. The post-fit nuisance parameter values, uncertainties, and impacts on the fitted signal strength are shown in Fig. 20, the negative log-likelihood scan is shown in Fig. 15. The nuisance parameters with the strongest impact on the expected extracted signal strength are related to the bin-by-bin statistical uncertainty in the background estimation. The evolution of upper limits with varying confidence level (CL), derived with the CL_s technique [104, 105] using asymptotic approximations [106], is shown in Fig. 16.

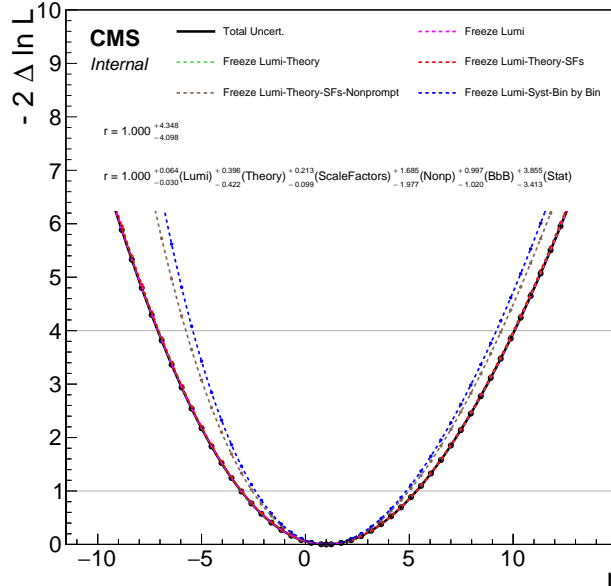


Figure 15: Negative log-likelihood profile of the signal+background fit to the signal+background Asimov dataset.

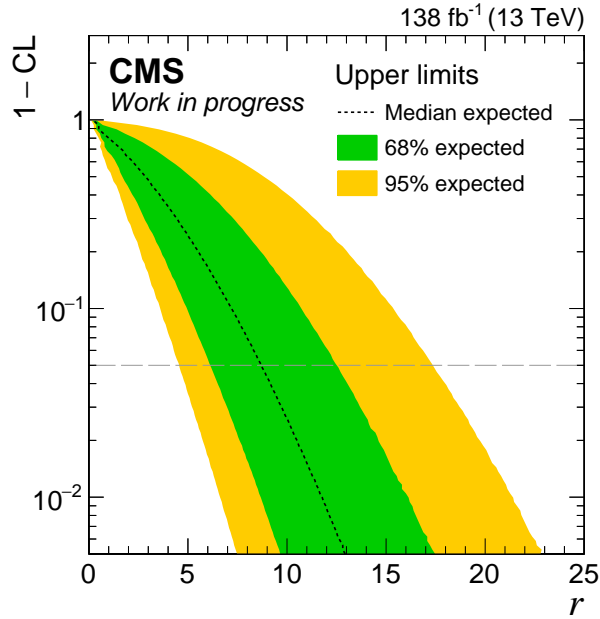


Figure 16: The upper limits on the signal strength using the CL_s method with the signal+background Asimov dataset.

8.3 Bias test and goodness of fit

The bias of the fit is checked using toy models generated with the `Higgs Combine` tool with expected signal rates of 0 and 1 respectively. For each case, 10000 toy models are generated by fluctuating each bin of the Asimov dataset according to the pre-fit Poisson distribution. The distributions of the normalized difference between the fitted and input signal rate, calculated for each toy dataset, are shown in Fig. 17 for an injected signal rate of 0 and 1, respectively. Both distributions are clearly Gaussian with mean values and standard deviations very close to 0 and 1, respectively, which means the fit is unbiased. The negative mean value is expected, as many nuisance parameters are constrained by asymmetric log-normal distributions in the fit.

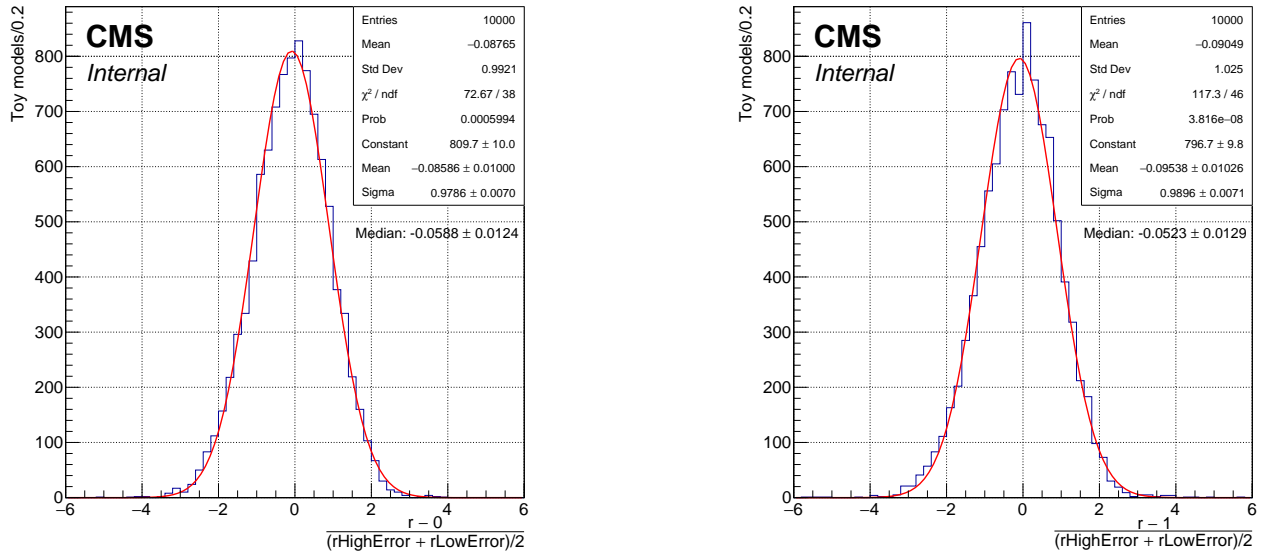


Figure 17: Bias check for toy models without signal ($r = 0$, left) and with signal ($r = 1$, right).

The goodness of fit is also studied using 1000 toy models based on the saturated model method [107]. The distribution of the goodness-of-fit measure is shown in Fig. 18 with the blue arrow indicating the value computed with real data. The p -value defined as the proportion of the values from the toy model that lie to the right of the value from the data is 0.142, which means the data is well-compatible with the simulation modeling.

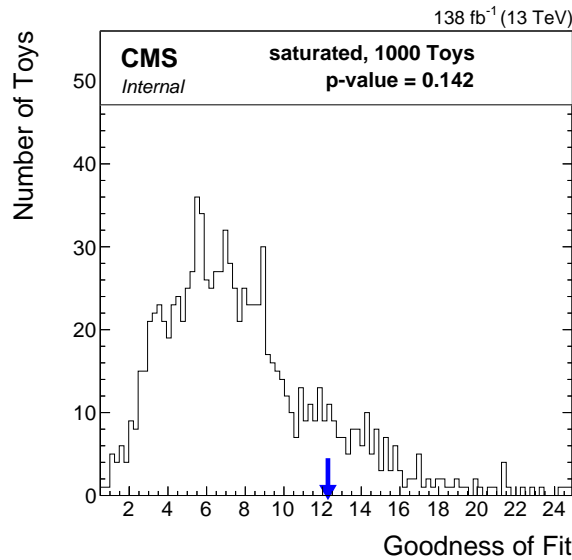


Figure 18: The distribution of the goodness-of-fit measure

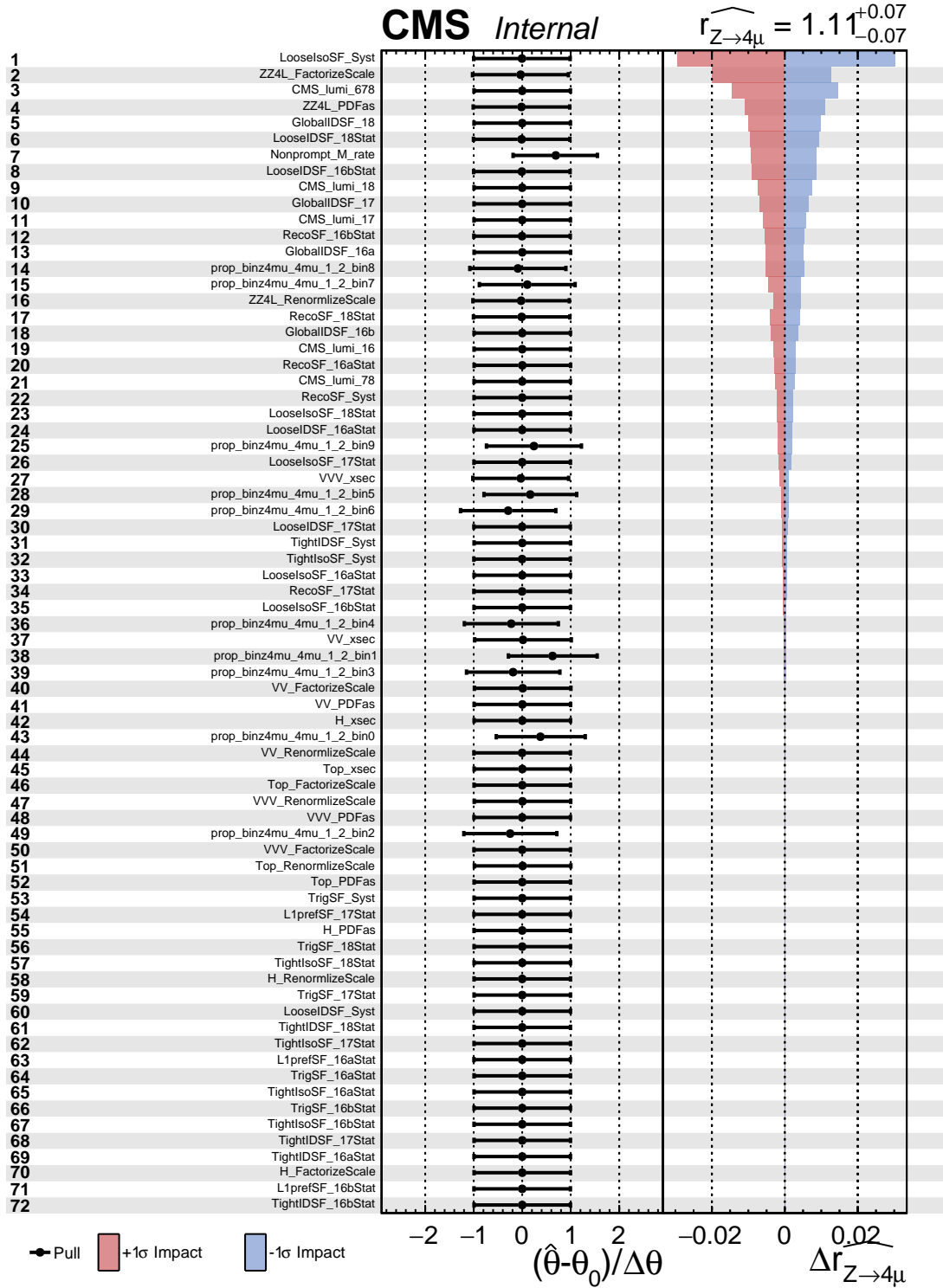


Figure 19: Post-fit nuisance parameters, uncertainties, and impacts of the background-only fit. The 2016 pre-VFP and 2016 post-VFP eras are noted as 16a and 16b here for short.

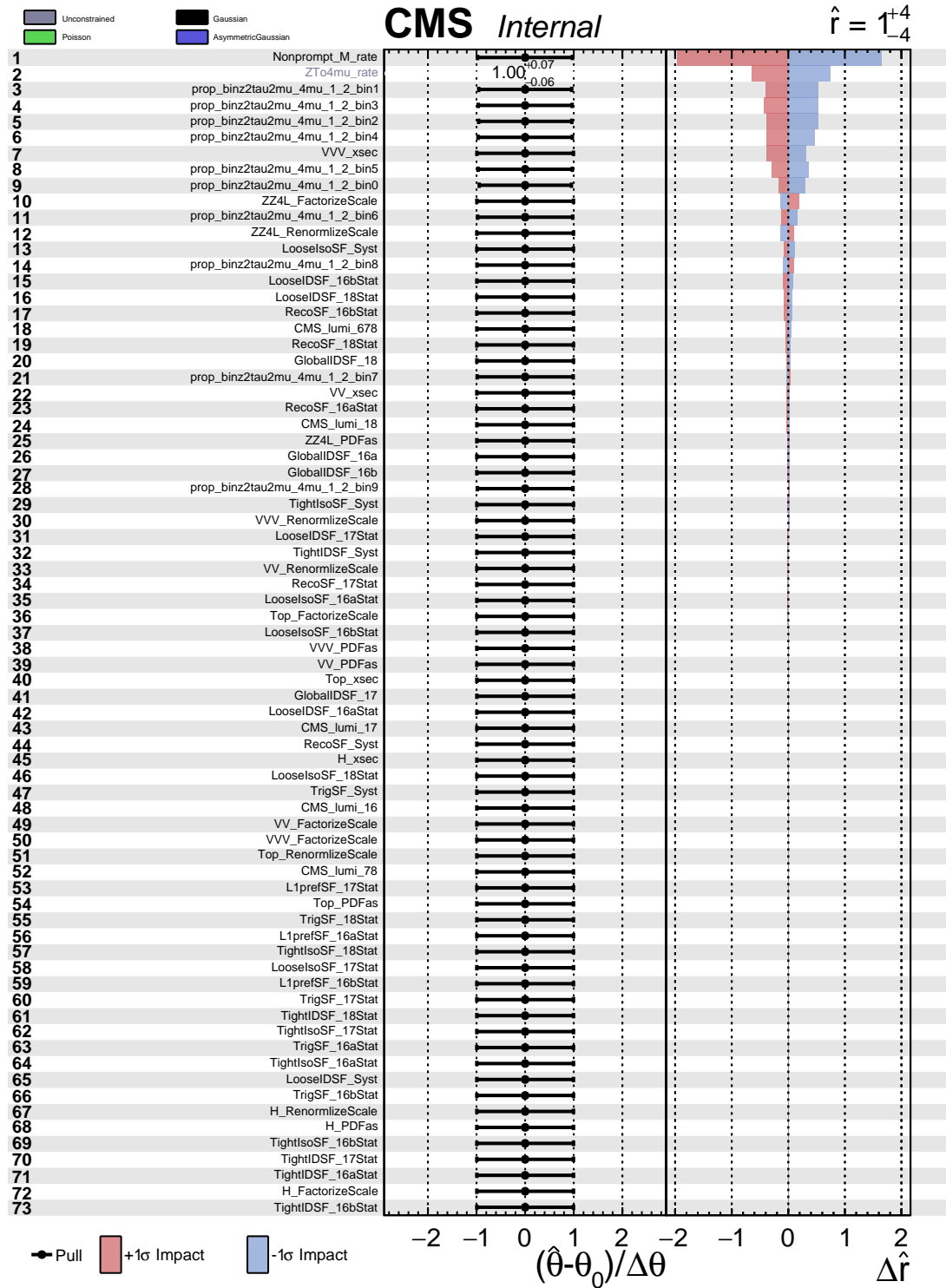


Figure 20: Post-fit nuisance parameters, uncertainties, and impacts from fit on the signal+background Asimov dataset. The 2016 pre-VFP and 2016 post-VFP eras are noted as 16a and 16b for short.

9 Results

9.1 Acceptance and efficiency

The phase space for both the signal and reference channels is defined by the requirements imposed on the four-muon invariant mass. They are $12 < m_{Z_1} < 75 \text{ GeV}$, $m_{Z_2} > 4 \text{ GeV}$, and the four-muon invariant mass to be between $40 < m_{\mu^+\mu^-\mu^+\mu^-} < 100 \text{ GeV}$. The phase space and detector regions are summarized in Table 7. The p_T cut for the leading muon for 2017 is $p_T^{\mu_1} > 29 \text{ GeV}$. The phase space region is defined using MC-truth quantities, while the detector region uses reconstructed-level quantities.

Table 7: Phase space and detector level region definitions for the $Z \rightarrow \tau^+\tau^-\mu^+\mu^-$ measurement.

Phase space	$40 < m_{\mu^+\mu^-\mu^+\mu^-} < 100 \text{ GeV}$ $m_{\mu^+\mu^-} > 4 \text{ GeV}$ and $12 < m_{Z_1} < 75 \text{ GeV}$
Detector region	$p_T^{\mu_1} > 26 \text{ GeV}$, $p_T^{\mu_2} > 3.5 \text{ GeV}$, $p_T^{\mu_3} > 3.5 \text{ GeV}$ $p_T^{\mu_4} > 3.5 \text{ GeV}$ for $ \eta^{\mu_4} < 1.2$ and $p_T^{\mu_4} > 2.5 \text{ GeV}$ for $ \eta^{\mu_4} > 1.2$ $ \eta^{\mu} < 2.4$

For the $Z \rightarrow \tau^+\tau^-\mu^+\mu^-$ and $Z \rightarrow \mu^+\mu^-\mu^+\mu^-$ processes, the acceptance A and efficiencies ϵ are obtained from simulation using the ZZT04L samples. The results are in Table 8, where the uncertainties are purely statistical. The acceptance is calculated as the ratio of events $N_{\text{detector}}/N_{\text{generator}}$, where $N_{\text{generator}}$ is the number of events in the phase space. The N_{detector} is the number out of the $N_{\text{generator}}$ events that have four truth-matched reconstructed muons falling in the detector region. The efficiency is calculated as $N_{\text{selected}}/N_{\text{detector}}$, where N_{selected} is the number of events matched with truth-level muons and passing the event and trigger selections described in chapter 5. The numbers of events are corrected for all the scale factors. The acceptances and efficiencies are cross-checked with the values obtained using the ZZT04LM-1toInf samples following the same selections as shown in Table 13. They are found to be compatible.

Table 8: Efficiency and acceptance of the two decay modes per year of data taking.

Year	$A_{Z \rightarrow \mu^+\mu^-\mu^+\mu^-}$	$\epsilon_{Z \rightarrow \mu^+\mu^-\mu^+\mu^-}$	$A_{Z \rightarrow \tau^+\tau^-\mu^+\mu^-}$	$\epsilon_{Z \rightarrow \tau^+\tau^-\mu^+\mu^-}$
2016 preVFP	0.1653 ± 0.0003	0.4004 ± 0.0008	0.0649 ± 0.0010	0.2522 ± 0.0071
2016 postVFP	0.1700 ± 0.0003	0.4064 ± 0.0008	0.0659 ± 0.0010	0.2609 ± 0.0069
2017	0.1534 ± 0.0002	0.3752 ± 0.0006	0.0469 ± 0.0006	0.1936 ± 0.0054
2018	0.1713 ± 0.0002	0.3875 ± 0.0006	0.0647 ± 0.0007	0.2146 ± 0.0048

9.2 Non-resonant factor

This analysis aims at measuring the singly-resonant modes of the $Z \rightarrow \tau^+\tau^-\mu^+\mu^-$ and $Z \rightarrow \mu^+\mu^-\mu^+\mu^-$ processes as shown in Fig. 21 (a), which shows an s -channel production.

However, there are also non-resonant processes participating in the four-lepton final state as shown in Fig. 21 (b). The number of events for contributions that are not due to singly-resonant production are corrected with a factor $(1 - f_\mu)/(1 - f_\tau)$ in the branching ratio formula. Here, f_μ and f_τ are the fractions of $pp \rightarrow \mu^+\mu^-\mu^+\mu^-$ and $pp \rightarrow \tau^+\tau^-\mu^+\mu^-$ events that come from s -channel Z boson production. The gluon-initiated doubly resonant ZZ production is not included in the simulated samples and is not considered in the following, it is negligible compared to the quark-initiated process.

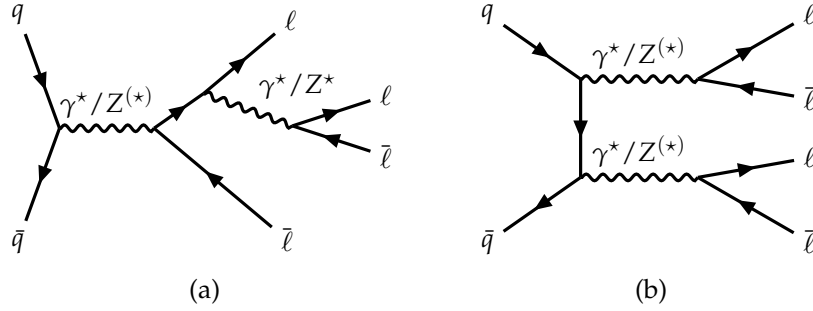


Figure 21: Resonant (a) and non-resonant (b) four lepton final state processes.

The correction follows a similar approach as the one used in Ref. [8] in order to estimate the fraction of events that are due to doubly-resonant processes. The cross sections are computed with `MadGraph_aMC@NLO v2.7` at the leading order for different processes, in all cases using identical generator-level cuts in line with the phase space of this analysis. Finally, an MC-sample-based validation of the f_τ result is performed in order to cross-check the numerical computation.

Nominal result: Cross-section-based estimate

The cross sections are computed for the inclusive four-lepton production, $pp \rightarrow \mu^+\mu^-\mu^+\mu^-$ and $pp \rightarrow \tau^+\tau^-\mu^+\mu^-$, and for the doubly-resonant on-shell production of $pp \rightarrow ZZ$, $pp \rightarrow Z\gamma$, and $pp \rightarrow \gamma\gamma$, and finally for the singly-resonant Z boson production, $pp \rightarrow Z$. The gauge bosons decay either to a final state with two muons and two τ leptons or promptly to four muons.

The ratio of the singly-resonant cross section to the inclusive one is defined as f_τ ($2\tau + 2\mu$ final state) and f_μ (4μ final state). All cross sections are computed with the following generator-level cuts applied at the level of `MadGraph` cards:

- $p_T^\ell > 1 \text{ GeV}$, where here ℓ refers to muons or τ leptons.
- $M_{\ell^+\ell^-} > 4 \text{ GeV}$ for all pairs of same-flavor, opposite-sign muons or τ leptons.
- $M_{4\ell} \in [40, 100] \text{ GeV}$, which refers to the invariant mass of the four leptons produced on generator-level, either $\tau^+\tau^-\mu^+\mu^-$ or $\mu^+\mu^-\mu^+\mu^-$

The corresponding LO cross sections for the four processes, as well as the values of f_μ and f_τ , are listed in Table 9. The resulting factor used in the calculation of the branching

fraction is therefore

$$\frac{f_\tau}{f_\mu} = \frac{0.839 \pm 0.001}{0.855 \pm 0.002} = 0.982 \pm 0.002 \quad (9.1)$$

Table 9: LO cross sections for inclusive and singly-resonant production of either $2\tau + 2\mu$ or 4μ , along with their ratio. The uncertainty in the cross section is the statistical uncertainty. The error on f is obtained by Gaussian error propagation.

Final state	Inclusive σ [fb]	Singly-res. σ [fb]	Singly res. fraction f
$2\tau + 2\mu$	109.0 ± 0.1	91.48 ± 0.08	$f_\tau = 0.839 \pm 0.001$
4μ	56.7 ± 0.1	48.46 ± 0.04	$f_\mu = 0.855 \pm 0.002$

Validation I: small effect of interference

In order to quantify the impact of potential interference between the singly- and doubly-resonant processes, it is instructive to consider the sum of singly- and doubly-resonant cross sections and the inclusive one. The difference should be due to the interference. The corresponding values are shown in Table 10.

Table 10: LO cross sections for inclusive as well as singly- and doubly- resonant production of either $2\tau + 2\mu$ or 4μ , and their differences, which represent the interference of the two production modes. The uncertainty in the cross section is the statistical uncertainty.

Final state	Incl. σ [fb]	Doubly res. σ [fb]	Singly-res. σ [fb]	Incl. - (Sing. + Doub.) [fb]
$2\tau + 2\mu$	109.0 ± 0.1	13.70 ± 0.01	91.48 ± 0.08	$3.82 = 3.5\%$
4μ	56.7 ± 0.1	7.33 ± 0.01	48.46 ± 0.04	$0.91 = 1.6\%$

It is evident that the sum of singly- and doubly-resonant cross sections do not differ from the inclusive one by more than 3.5%, showing that the influence of interference is small in this analysis. In order to verify this conclusion, the singly-resonant factors are compared with $(1 - f^{\text{DR}})$, where f^{DR} is the ratio of the doubly-resonant and the inclusive cross sections. Since the interference effect is small (but not 0), the ratio $(1 - f_\tau^{\text{DR}})/(1 - f_\mu^{\text{DR}})$ must be similar (but not the same) to the ratio derived in the previous section. The ingredients to this calculation are shown in Table 11.

Table 11: LO cross sections for inclusive, singly, and doubly resonant production of either $2\tau + 2\mu$ or 4μ , along with their ratio. The uncertainty in the cross section is the statistical uncertainty. The error on f is obtained by Gaussian error propagation.

Final state	Inclusive σ [fb]	Doubly-res. σ [fb]	Doubly-resonant fraction f^{DR}
$2\tau + 2\mu$	109.0 ± 0.1	13.70 ± 0.01	$f_\tau^{\text{DR}} = 0.1257 \pm 0.0002$
4μ	56.7 ± 0.1	7.33 ± 0.01	$f_\mu^{\text{DR}} = 0.1293 \pm 0.0003$

The resulting correction factor would be:

$$\frac{1 - f_\tau^{\text{DR}}}{1 - f_\mu^{\text{DR}}} = 1.004 \pm 0.002. \quad (9.2)$$

This correction factor is, as expected, very close to the one derived as the nominal result in the previous section. However, since it neglects the different interference terms, it differs slightly from what is used as the nominal result. The interference effect is larger in the $\tau^+\tau^-\mu^+\mu^-$ channel, thus the resulting factor is slightly larger than what is used nominally.

Validation II: MC-sample-based estimate

In order to validate the computations performed at LO by MadGraph5, a sample of simulated resonant $pp \rightarrow Z \rightarrow \tau^+\tau^-\mu^+\mu^-$ events is produced privately with MadGraph_aMC@NLO v2.7 at LO. We compare the number of truth-level events in this sample falling in the phase space and detector region defined in Table 7 to the number of $pp \rightarrow \tau^+\tau^-\mu^+\mu^-$ events from the inclusive ZZTo4L sample passing the same selections. A shape comparison in the signal region ($M_{4\ell} \in [40, 100]$ GeV) of both samples is shown in Fig. 22, where it is evident that the shapes of the central (inclusive) and private (s-channel only) samples agree very well up to an invariant mass of about 80 GeV. At higher values, the difference between both shapes is due to the presence of non-s-channel processes.

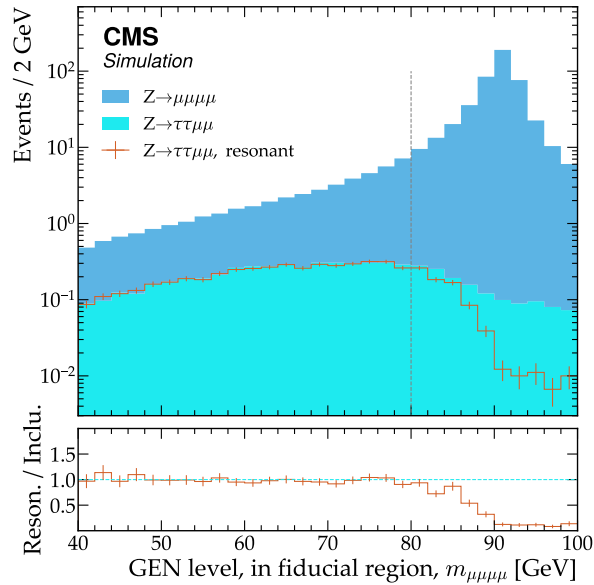


Figure 22: Generator level four muon invariant mass distribution in the CMS fiducial region.

In order to estimate again the fraction of these non-s-channel processes, two steps are taken. The first step is to normalize both distributions to have the same integral in the reconstructed invariant mass range of 40–80 GeV, where the s-channel process dominates. The second is to compute the ratio of integrals of both distributions (after normalizing them in the first step) over the full invariant mass range 40–100 GeV as:

$$f_\tau = \frac{\text{Integral (s-channel only)}}{\text{Integral (inclusive)}} = 0.890 \pm 0.008. \quad (9.3)$$

This number is very close to the one computed when deriving the nominal result. Differences can occur due to the different order at which the central Powheg and the private MadGraph5 sample were produced and the normalization in the first step based on the assumption that the [40, 80] GeV mass range is dominated by the s -channel. However, it is not expected that significant differences arise between the $\tau^+\tau^-\mu^+\mu^-$ and $\mu^+\mu^-\mu^+\mu^-$ final states. The number is cross-checked with the same value obtained using the ZZTo4LM-1toInf sample.

9.3 Branching fraction measurement

The branching fraction of the $Z \rightarrow \tau^+\tau^-\mu^+\mu^-$ process, relative to that of the $Z \rightarrow \mu^+\mu^-\mu^+\mu^-$ process, is measured using the formula:

$$\frac{\mathcal{B}(Z \rightarrow \tau^+\tau^-\mu^+\mu^-)}{\mathcal{B}(Z \rightarrow \mu^+\mu^-\mu^+\mu^-)} = \frac{r \times r_{Z \rightarrow 4\mu} \times N^{\text{SM}}(Z \rightarrow \tau^+\tau^-\mu^+\mu^-)}{r_{Z \rightarrow 4\mu} \times N^{\text{SM}}(Z \rightarrow \mu^+\mu^-\mu^+\mu^-)} \times \frac{(A \times \epsilon)_{Z \rightarrow \mu^+\mu^-\mu^+\mu^-}}{(A \times \epsilon)_{Z \rightarrow \tau^+\tau^-\mu^+\mu^-}} \frac{1}{\mathcal{B}^2(\tau^\pm \rightarrow \mu^\pm)} \frac{f_\tau}{f_\mu}. \quad (9.4)$$

The signal and background yields are shown in Table 12. The parameters f_μ and f_τ correct for the fraction of selected $\tau^+\tau^-\tau^+\tau^-$ and $\mu^+\mu^-\tau^+\tau^-$ events not due to s -channel Z boson exchange, respectively, as explained in more detail in the previous section. The ratio f_τ/f_μ is 0.982 ± 0.002 . The branching fraction of τ leptons decay to muons is $\mathcal{B}(\tau \rightarrow \mu) = (17.39 \pm 0.04) \times 10^{-2}$ [108].

Table 12: The expected number of events. The uncertainty includes statistics and systematics. Note that the $Z \rightarrow \tau^+\tau^-\mu^+\mu^- \rightarrow \mu^+\mu^-\mu^+\mu^-$ yield shown in the plots is multiplied by 5 for visualization only, which is indicated by “ $\times 5$ ” in the legend. The number here corresponds to the nominal ($\times 1$ instead of $\times 5$) input to combine.

Process	N_{exp}
$Z \rightarrow \tau^+\tau^-\mu^+\mu^- \rightarrow \mu^+\mu^-\mu^+\mu^-$	2.61 ± 0.04
$Z \rightarrow \mu^+\mu^-\mu^+\mu^-$	458.41 ± 13.88
Non-prompt muons	29.87 ± 7.89
H	0.67 ± 0.02
VVV	5.86 ± 0.68
VV	1.70 ± 0.23
Top	1.06 ± 0.17
Total	500.18 ± 15.98

Setting the r as 1, the ratio is expected to be

$$\left(\frac{\mathcal{B}(Z \rightarrow \tau^+ \tau^- \mu^+ \mu^-)}{\mathcal{B}(Z \rightarrow \mu^+ \mu^- \mu^+ \mu^-)} \right)_{\text{SM}} = 0.902 \pm_{-3.212}^{+3.590} (\text{stat.}) \pm_{-1.825}^{+1.574} (\text{syst.}). \quad (9.5)$$

At the time of writing, the analysis is already pre-approved by the CMS Standard Model Physics group, yet the result fitted with real data remains blinded. After unblinding, the absolute branching fraction of the $Z \rightarrow \tau^+ \tau^- \mu^+ \mu^-$ in the phase space defined in section 9.1 can be derived with the ratio and the measured branching fraction $\mathcal{B}(Z \rightarrow \mu^+ \mu^- \mu^+ \mu^-) = (4.63 \pm 0.21) \times 10^{-6}$ [108].

10 Summary

This thesis presents the first dedicated $Z \rightarrow \tau^+ \tau^- \mu^+ \mu^-$ decay analysis in the muon decay mode of the τ leptons and sets an upper limit on the branching fraction $\mathcal{B}(Z \rightarrow \tau^+ \tau^- \mu^+ \mu^-)$. This analysis uses cut-based event selections and data recorded at a center of mass energy of $\sqrt{s} = 13$ TeV by the CMS detector from 2016 to 2018 corresponding to an integrated luminosity of 138 fb^{-1} . The main source of background comes from the $Z \rightarrow \mu^+ \mu^- \mu^+ \mu^-$ and it is treated as a reference channel. The background consisting of non-prompt muons is estimated with a data-driven method. The signal yield is extracted from a binned maximum-likelihood fit to the data.

This result can contribute to the constraints on the untested SMEFT Wilson coefficients of four lepton operators involving tau leptons and the Z' and $L_\mu - L_\tau$ BSM models. For further studies, one can generate MC samples with new physics models or new operators and test the sensitivity of this channel. On the other hand, one can also compare the expected sensitivity with the theoretical derivation on the branching fraction induced by the new physics models, which needs dedicated calculations. This channel is also a background to Higgs boson leptonic decays.

The analysis can be extended with other decay modes of the τ lepton. For the electron decay mode, the easiest extension would be to replace the high- p_T and trigger muon with a high- p_T electron. This way, one could probe the final state where the τ leptons are coupled to the on-shell Z with one decaying to an electron and another going to muons. Although the final state of $Z \rightarrow \tau\tau\mu\mu \rightarrow e\mu\mu\mu$ will have less statistics, as it ignores the τ leptons coming from the off-shell γ/Z , it is much cleaner with respect to backgrounds, as it reduces non-prompt muons and combinatorics. Analyses with low p_T electrons are also possible, but they would require more complicated techniques as the reconstruction and identification efficiency for low p_T electrons in CMS is not very high. Finally, as the analysis is dominated by statistics, it is expected that it will be improved a lot with the data collected in the Run 3 period of LHC.

Acknowledgements

I would like to express my sincere gratitude to Prof. Benjamin Kilminster for providing me with the opportunity to conduct this project and write my master's thesis within his research group. I would also like to thank Dr. Stefanos Leontsinis and Dr. Arne Reimers for their guidance and supervision throughout the project. Their support and insights have been invaluable to me. I would also like to extend my appreciation to Dr. Yuta Takahashi and Dr. Izaak Neutelings for their help and sharp comments. It was a pleasure for me to be in a group where everyone was open to my questions. Finally, I would like to express my appreciation to my family and friends for their support and encouragement throughout this journey.

References

- [1] S. L. Glashow. “Partial Symmetries of Weak Interactions”. In: *Nucl. Phys.* 22 (1961), pp. 579–588. DOI: 10.1016/0029-5582(61)90469-2.
- [2] Steven Weinberg. “A Model of Leptons”. In: *Phys. Rev. Lett.* 19 (1967), pp. 1264–1266. DOI: 10.1103/PhysRevLett.19.1264.
- [3] Abdus Salam. “Weak and Electromagnetic Interactions”. In: *Conf. Proc. C* 680519 (1968), pp. 367–377. DOI: 10.1142/9789812795915_0034.
- [4] CMS Collaboration. “The CMS experiment at the CERN LHC”. In: *JINST* 3 (2008), S08004. DOI: 10.1088/1748-0221/3/08/S08004.
- [5] “LHC Machine”. In: *JINST* 3 (2008). Ed. by Lyndon Evans and Philip Bryant, S08001. DOI: 10.1088/1748-0221/3/08/S08001.
- [6] CMS Collaboration. “Observation of the $Z \rightarrow \psi \ell^+ \ell^-$ decay in pp collisions at $\sqrt{s} = 13$ TeV”. In: *Phys. Rev. Lett.* 121 (2018), p. 141801. DOI: 10.1103/PhysRevLett.121.141801. arXiv: 1806.04213 [hep-ex].
- [7] CMS Collaboration. “Observation of Z Decays to Four Leptons with the CMS Detector at the LHC”. In: *JHEP* 12 (2012), p. 034. DOI: 10.1007/JHEP12(2012)034. arXiv: 1210.3844 [hep-ex].
- [8] CMS Collaboration. “Measurements of the $pp \rightarrow ZZ$ production cross section and the $Z \rightarrow 4\ell$ branching fraction, and constraints on anomalous triple gauge couplings at $\sqrt{s} = 13$ TeV”. In: *Eur. Phys. J. C* 78 (2018). [Erratum: *Eur.Phys.J.C* 78, 515 (2018)], p. 165. DOI: 10.1140/epjc/s10052-018-5567-9. arXiv: 1709.08601 [hep-ex].
- [9] Radja Boughezal et al. “Four-lepton Z boson decay constraints on the standard model EFT”. In: *Phys. Rev. D* 103.5 (2021), p. 055015. DOI: 10.1103/PhysRevD.103.055015. arXiv: 2010.06685 [hep-ph].
- [10] Paul Langacker. “The Physics of Heavy Z' Gauge Bosons”. In: *Rev. Mod. Phys.* 81 (2009), pp. 1199–1228. DOI: 10.1103/RevModPhys.81.1199. arXiv: 0801.1345 [hep-ph].
- [11] Xiao-Gang He et al. “Simplest Z' model”. In: *Phys. Rev. D* 44 (7 1991), pp. 2118–2132. DOI: 10.1103/PhysRevD.44.2118. URL: <https://link.aps.org/doi/10.1103/PhysRevD.44.2118>.
- [12] CMS Collaboration. “Measurements of properties of the Higgs boson decaying into the four-lepton final state in pp collisions at $\sqrt{s} = 13$ TeV”. In: *JHEP* 11 (2017), p. 047. DOI: 10.1007/JHEP11(2017)047. arXiv: 1706.09936 [hep-ex].
- [13] Wikipedia. *Standard Model* — *Wikipedia*. <http://en.wikipedia.org/w/index.php?title=Standard%20Model&oldid=1114254138>. [Online; accessed 27-October-2022]. Nov. 2022.

- [14] Peter W. Higgs. “Broken Symmetries and the Masses of Gauge Bosons”. In: *Phys. Rev. Lett.* 13 (1964). Ed. by J. C. Taylor, pp. 508–509. DOI: 10.1103/PhysRevLett.13.508.
- [15] F. Englert and R. Brout. “Broken Symmetry and the Mass of Gauge Vector Mesons”. In: *Phys. Rev. Lett.* 13 (1964). Ed. by J. C. Taylor, pp. 321–323. DOI: 10.1103/PhysRevLett.13.321.
- [16] T. W. B. Kibble. “Symmetry breaking in nonAbelian gauge theories”. In: *Phys. Rev.* 155 (1967). Ed. by J. C. Taylor, pp. 1554–1561. DOI: 10.1103/PhysRev.155.1554.
- [17] G. S. Guralnik, C. R. Hagen, and T. W. B. Kibble. “Global Conservation Laws and Massless Particles”. In: *Phys. Rev. Lett.* 13 (1964). Ed. by J. C. Taylor, pp. 585–587. DOI: 10.1103/PhysRevLett.13.585.
- [18] CMS Collaboration. “Observation of a New Boson at a Mass of 125 GeV with the CMS Experiment at the LHC”. In: *Phys. Lett. B* 716 (2012), pp. 30–61. DOI: 10.1016/j.physletb.2012.08.021. arXiv: 1207.7235 [hep-ex].
- [19] ATLAS Collaboration. “Observation of a new particle in the search for the Standard Model Higgs boson with the ATLAS detector at the LHC”. In: *Phys. Lett. B* 716 (2012), pp. 1–29. DOI: 10.1016/j.physletb.2012.08.020. arXiv: 1207.7214 [hep-ex].
- [20] “Test of lepton universality with $B^0 \rightarrow K^{*0} \ell^+ \ell^-$ decays”. In: *JHEP* 08 (2017), p. 055. DOI: 10.1007/JHEP08(2017)055. arXiv: 1705.05802 [hep-ex].
- [21] “Search for lepton-universality violation in $B^+ \rightarrow K^+ \ell^+ \ell^-$ decays”. In: *Phys. Rev. Lett.* 122 (2019), p. 191801. DOI: 10.1103/PhysRevLett.122.191801. arXiv: 1903.09252 [hep-ex].
- [22] “Test of Lepton-Flavor Universality in $B \rightarrow K^* \ell^+ \ell^-$ Decays at Belle”. In: *Phys. Rev. Lett.* 126 (2021), p. 161801. DOI: 10.1103/PhysRevLett.126.161801. arXiv: 1904.02440 [hep-ex].
- [23] LHCb Collaboration. “Test of lepton universality in beauty-quark decays”. In: *Nature Phys.* 18.3 (2022), pp. 277–282. DOI: 10.1038/s41567-021-01478-8. arXiv: 2103.11769 [hep-ex].
- [24] LHCb Collaboration. “Tests of lepton universality using $B^0 \rightarrow K_S^0 \ell^+ \ell^-$ and $B^+ \rightarrow K^{*+} \ell^+ \ell^-$ decays”. In: *Phys. Rev. Lett.* 128.19 (2022), p. 191802. DOI: 10.1103/PhysRevLett.128.191802. arXiv: 2110.09501 [hep-ex].
- [25] Belle Collaboration. “Recent Results on Lepton Flavor Universality Test at Belle”. In: *Springer Proc. Phys.* 277 (2022), pp. 231–235. DOI: 10.1007/978-981-19-2354-8_42.
- [26] “Test of lepton universality in $b \rightarrow s \ell^+ \ell^-$ decays”. In: (Dec. 2022). arXiv: 2212.09152 [hep-ex].
- [27] Seungwon Baek et al. “Muon anomalous $g - 2$ and gauged $L_\mu - L_\tau$ models”. In: *Phys. Rev. D* 64 (2001), p. 055006. DOI: 10.1103/PhysRevD.64.055006. arXiv: hep-ph/0104141.
- [28] Andrzej J. Buras et al. “Global analysis of leptophilic Z' bosons”. In: *JHEP* 06 (2021), p. 068. DOI: 10.1007/JHEP06(2021)068. arXiv: 2104.07680 [hep-ph].

- [29] P. Ko, Takaaki Nomura, and Hiroshi Okada. “Muon $g - 2$, $B \rightarrow K^{(*)} \mu^+ \mu^-$ anomalies, and leptophilic dark matter in $U(1)_{\mu-\tau}$ gauge symmetry”. In: *JHEP* 05 (2022), p. 098. DOI: 10.1007/JHEP05(2022)098. arXiv: 2110.10513 [hep-ph].
- [30] Francisco del Aguila et al. “Collider limits on leptophilic interactions”. In: *JHEP* 03 (2015), p. 059. DOI: 10.1007/JHEP03(2015)059. arXiv: 1411.7394 [hep-ph].
- [31] Fatemeh Elahi and Adam Martin. “Constraints on $L_\mu - L_\tau$ interactions at the LHC and beyond”. In: *Phys. Rev. D* 93.1 (2016), p. 015022. DOI: 10.1103/PhysRevD.93.015022. arXiv: 1511.04107 [hep-ph].
- [32] Fatemeh Elahi and Adam Martin. “Using the modified matrix element method to constrain $L_\mu - L_\tau$ interactions”. In: *Phys. Rev. D* 96.1 (2017), p. 015021. DOI: 10.1103/PhysRevD.96.015021. arXiv: 1705.02563 [hep-ph].
- [33] Stephen F. King. “Flavourful Z' models for $R_{K^{(*)}}$ ”. In: *JHEP* 08 (2017), p. 019. DOI: 10.1007/JHEP08(2017)019. arXiv: 1706.06100 [hep-ph].
- [34] CMS Collaboration. “Search for an $L_\mu - L_\tau$ gauge boson using $Z \rightarrow 4\mu$ events in proton-proton collisions at $\sqrt{s} = 13$ TeV”. In: *Phys. Lett. B* 792 (2019), pp. 345–368. DOI: 10.1016/j.physletb.2019.01.072. arXiv: 1808.03684 [hep-ex].
- [35] Kento Asai. “Predictions for the neutrino parameters in the minimal model extended by linear combination of $U(1)_{L_e-L_\mu}$, $U(1)_{L_\mu-L_\tau}$ and $U(1)_{B-L}$ gauge symmetries”. In: *Eur. Phys. J. C* 80.2 (2020), p. 76. DOI: 10.1140/epjc/s10052-020-7622-6. arXiv: 1907.04042 [hep-ph].
- [36] Syuhei Iguro, Kirtimaan A. Mohan, and C. P. Yuan. “Detecting a $\mu\tau$ -philic Z' boson via photon initiated processes at the LHC”. In: *Phys. Rev. D* 101.7 (2020), p. 075011. DOI: 10.1103/PhysRevD.101.075011. arXiv: 2001.09079 [hep-ph].
- [37] Dorian Warren Praia do Amaral et al. “Solar neutrino probes of the muon anomalous magnetic moment in the gauged $U(1)_{L_\mu-L_\tau}$ ”. In: *JHEP* 12 (2020), p. 155. DOI: 10.1007/JHEP12(2020)155. arXiv: 2006.11225 [hep-ph].
- [38] G. Charpak et al. “A new measurement of the anomalous magnetic moment of the muon”. In: *Physics Letters* 1.1 (1962), pp. 16–20. ISSN: 0031-9163. DOI: [https://doi.org/10.1016/0031-9163\(62\)90263-9](https://doi.org/10.1016/0031-9163(62)90263-9). URL: <https://www.sciencedirect.com/science/article/pii/0031916362902639>.
- [39] J. Bailey et al. “Precision measurement of the anomalous magnetic moment of the muon”. In: *Physics Letters B* 28.4 (1968), pp. 287–290. ISSN: 0370-2693. DOI: [https://doi.org/10.1016/0370-2693\(68\)90261-X](https://doi.org/10.1016/0370-2693(68)90261-X). URL: <https://www.sciencedirect.com/science/article/pii/037026936890261X>.
- [40] J. Bailey et al. “Final report on the CERN muon storage ring including the anomalous magnetic moment and the electric dipole moment of the muon, and a direct test of relativistic time dilation”. In: *Nuclear Physics B* 150 (1979), pp. 1–75. ISSN: 0550-3213. DOI: [https://doi.org/10.1016/0550-3213\(79\)90292-X](https://doi.org/10.1016/0550-3213(79)90292-X). URL: <https://www.sciencedirect.com/science/article/pii/055032137990292X>.

- [41] Muon g-2 Collaboration. “Final Report of the Muon E821 Anomalous Magnetic Moment Measurement at BNL”. In: *Phys. Rev. D* 73 (2006), p. 072003. DOI: 10.1103/PhysRevD.73.072003. arXiv: hep-ex/0602035.
- [42] Muon g-2 Collaboration. “Measurement of the Positive Muon Anomalous Magnetic Moment to 0.46 ppm”. In: *Phys. Rev. Lett.* 126.14 (2021), p. 141801. DOI: 10.1103/PhysRevLett.126.141801. arXiv: 2104.03281 [hep-ex].
- [43] Nicole F. Bell et al. “Leptophilic dark matter with Z' interactions”. In: *Phys. Rev. D* 90.3 (2014), p. 035027. DOI: 10.1103/PhysRevD.90.035027. arXiv: 1407.3001 [hep-ph].
- [44] Wolfgang Altmannshofer et al. “Explaining dark matter and B decay anomalies with an $L_\mu - L_\tau$ model”. In: *JHEP* 12 (2016), p. 106. DOI: 10.1007/JHEP12(2016)106. arXiv: 1609.04026 [hep-ph].
- [45] Patrick Foldenauer. “Light dark matter in a gauged $U(1)_{L_\mu - L_\tau}$ model”. In: *Phys. Rev. D* 99.3 (2019), p. 035007. DOI: 10.1103/PhysRevD.99.035007. arXiv: 1808.03647 [hep-ph].
- [46] Timothy Hapitas, Douglas Tuckler, and Yue Zhang. “General kinetic mixing in gauged $U(1)_{L_\mu - L_\tau}$ model for muon g-2 and dark matter”. In: *Phys. Rev. D* 105.1 (2022), p. 016014. DOI: 10.1103/PhysRevD.105.016014. arXiv: 2108.12440 [hep-ph].
- [47] ATLAS Collaboration. “The ATLAS Experiment at the CERN Large Hadron Collider”. In: *JINST* 3 (2008), S08003. DOI: 10.1088/1748-0221/3/08/S08003.
- [48] LHCb Collaboration. “The LHCb Detector at the LHC”. In: *JINST* 3 (2008), S08005. DOI: 10.1088/1748-0221/3/08/S08005.
- [49] ALICE Collaboration. “The ALICE experiment at the CERN LHC”. In: *JINST* 3 (2008), S08002. DOI: 10.1088/1748-0221/3/08/S08002.
- [50] CMS Collaboration. “Highlights from the Compact Muon Solenoid (CMS) Experiment”. In: *Universe* 5.1 (2019), p. 28. DOI: 10.3390/universe5010028. arXiv: 1901.05340 [hep-ex].
- [51] CMS Collaboration. “Description and performance of track and primary-vertex reconstruction with the CMS tracker”. In: *JINST* 9.10 (2014), P10009. DOI: 10.1088/1748-0221/9/10/P10009. arXiv: 1405.6569 [physics.ins-det].
- [52] CMS Tracker Group Collaboration. “The CMS Phase-1 Pixel Detector Upgrade”. In: *JINST* 16.02 (2021), P02027. DOI: 10.1088/1748-0221/16/02/P02027. arXiv: 2012.14304 [physics.ins-det].
- [53] CMS Collaboration. “Electron and photon reconstruction and identification with the CMS experiment at the CERN LHC”. In: *JINST* 16.05 (2021), P05014. DOI: 10.1088/1748-0221/16/05/P05014. arXiv: 2012.06888 [hep-ex].
- [54] CMS Collaboration. *Performance of the Pixel Luminosity Telescope for Luminosity Measurement at CMS during Run2*. Tech. rep. Geneva: CERN, 2019. URL: <https://cds.cern.ch/record/2797807>.

- [55] CMS Collaboration. “Precision luminosity measurement in proton-proton collisions at $\sqrt{s} = 13$ TeV in 2015 and 2016 at CMS”. In: *Eur. Phys. J. C* 81.9 (2021), p. 800. DOI: 10.1140/epjc/s10052-021-09538-2. arXiv: 2104.01927 [hep-ex].
- [56] CMS Collaboration. “CMS reconstruction improvement for the muon tracking by the RPC chambers”. In: *PoS RPC2012* (2012), p. 045. DOI: 10.1088/1748-0221/8/03/T03001. arXiv: 1209.2646 [physics.ins-det].
- [57] CMS Collaboration. “The Performance of the CMS Muon Detector in Proton-Proton Collisions at $\sqrt{s} = 7$ TeV at the LHC”. In: *JINST* 8 (2013), P11002. DOI: 10.1088/1748-0221/8/11/P11002. arXiv: 1306.6905 [physics.ins-det].
- [58] CMS Collaboration. “Performance of the CMS muon detector and muon reconstruction with proton-proton collisions at $\sqrt{s} = 13$ TeV”. In: *JINST* 13.06 (2018), P06015. DOI: 10.1088/1748-0221/13/06/P06015. arXiv: 1804.04528 [physics.ins-det].
- [59] CMS Collaboration. “Performance of the CMS muon trigger system in proton-proton collisions at $\sqrt{s} = 13$ TeV”. In: *JINST* 16 (2021), P07001. DOI: 10.1088/1748-0221/16/07/P07001. arXiv: 2102.04790 [hep-ex].
- [60] CMS Collaboration. “Performance of the CMS Level-1 trigger in proton-proton collisions at $\sqrt{s} = 13$ TeV”. In: *JINST* 15.10 (2020), P10017. DOI: 10.1088/1748-0221/15/10/P10017. arXiv: 2006.10165 [hep-ex].
- [61] CMS Collaboration. “The CMS trigger system”. In: *JINST* 12.01 (2017), P01020. DOI: 10.1088/1748-0221/12/01/P01020. arXiv: 1609.02366 [physics.ins-det].
- [62] CMS Collaboration. “CMS Trigger Improvements Towards Run II”. In: *Nucl. Part. Phys. Proc.* 273-275 (2016), pp. 1008–1013. DOI: 10.1016/j.nuclphysbps.2015.09.158.
- [63] CMS Collaboration. *CMS luminosity measurement for the 2017 data-taking period at $\sqrt{s} = 13$ TeV*. Tech. rep. Geneva: CERN, 2018. URL: <https://cds.cern.ch/record/2621960>.
- [64] CMS Collaboration. *CMS luminosity measurement for the 2018 data-taking period at $\sqrt{s} = 13$ TeV*. Tech. rep. Geneva: CERN, 2019. URL: <https://cds.cern.ch/record/2676164>.
- [65] Paolo Nason. “A New method for combining NLO QCD with shower Monte Carlo algorithms”. In: *JHEP* 11 (2004), p. 040. DOI: 10.1088/1126-6708/2004/11/040. arXiv: hep-ph/0409146.
- [66] Stefano Frixione, Paolo Nason, and Carlo Oleari. “Matching NLO QCD computations with Parton Shower simulations: the POWHEG method”. In: *JHEP* 11 (2007), p. 070. DOI: 10.1088/1126-6708/2007/11/070. arXiv: 0709.2092 [hep-ph].
- [67] Simone Alioli et al. “A general framework for implementing NLO calculations in shower Monte Carlo programs: the POWHEG BOX”. In: *JHEP* 06 (2010), p. 043. DOI: 10.1007/JHEP06(2010)043. arXiv: 1002.2581 [hep-ph].
- [68] Tom Melia et al. “W+W-, WZ and ZZ production in the POWHEG BOX”. In: *JHEP* 11 (2011), p. 078. DOI: 10.1007/JHEP11(2011)078. arXiv: 1107.5051 [hep-ph].

- [69] Paolo Nason and Giulia Zanderighi. “ W^+W^- , WZ and ZZ production in the POWHEG-BOX-V2”. In: *Eur. Phys. J. C* 74.1 (2014), p. 2702. DOI: 10.1140/epjc/s10052-013-2702-5. arXiv: 1311.1365 [hep-ph].
- [70] Stefano Frixione, Paolo Nason, and Giovanni Ridolfi. “A Positive-weight next-to-leading-order Monte Carlo for heavy flavour hadroproduction”. In: *JHEP* 09 (2007), p. 126. DOI: 10.1088/1126-6708/2007/09/126. arXiv: 0707.3088 [hep-ph].
- [71] J. Alwall et al. “The automated computation of tree-level and next-to-leading order differential cross sections, and their matching to parton shower simulations”. In: *JHEP* 07 (2014), p. 079. DOI: 10.1007/JHEP07(2014)079. arXiv: 1405.0301 [hep-ph].
- [72] Paolo Nason and Carlo Oleari. “NLO Higgs boson production via vector-boson fusion matched with shower in POWHEG”. In: *JHEP* 02 (2010), p. 037. DOI: 10.1007/JHEP02(2010)037. arXiv: 0911.5299 [hep-ph].
- [73] E. Bagnaschi et al. “Higgs production via gluon fusion in the POWHEG approach in the SM and in the MSSM”. In: *JHEP* 02 (2012), p. 088. DOI: 10.1007/JHEP02(2012)088. arXiv: 1111.2854 [hep-ph].
- [74] Yanyan Gao et al. “Spin Determination of Single-Produced Resonances at Hadron Colliders”. In: *Phys. Rev. D* 81 (2010), p. 075022. DOI: 10.1103/PhysRevD.81.075022. arXiv: 1001.3396 [hep-ph].
- [75] Sara Bolognesi et al. “On the spin and parity of a single-produced resonance at the LHC”. In: *Phys. Rev. D* 86 (2012), p. 095031. DOI: 10.1103/PhysRevD.86.095031. arXiv: 1208.4018 [hep-ph].
- [76] Ian Anderson et al. “Constraining Anomalous HVV Interactions at Proton and Lepton Colliders”. In: *Phys. Rev. D* 89.3 (2014). Ed. by Norman A. Graf, Michael E. Peskin, and Jonathan L. Rosner, p. 035007. DOI: 10.1103/PhysRevD.89.035007. arXiv: 1309.4819 [hep-ph].
- [77] CMS Collaboration. *Standard Model Cross Sections for CMS at 13 TeV*. <https://twiki.cern.ch/twiki/bin/viewauth/CMS/StandardModelCrossSectionsat13TeV>. Nov. 2022.
- [78] NNPDF Collaboration. “Parton distributions from high-precision collider data”. In: *Eur. Phys. J. C* 77.10 (2017), p. 663. DOI: 10.1140/epjc/s10052-017-5199-5. arXiv: 1706.00428 [hep-ph].
- [79] Andy Buckley et al. “General-purpose event generators for LHC physics”. In: *Phys. Rept.* 504 (2011), pp. 145–233. DOI: 10.1016/j.physrep.2011.03.005. arXiv: 1101.2599 [hep-ph].
- [80] Torbjorn Sjostrand, Stephen Mrenna, and Peter Z. Skands. “PYTHIA 6.4 Physics and Manual”. In: *JHEP* 05 (2006), p. 026. DOI: 10.1088/1126-6708/2006/05/026. arXiv: hep-ph/0603175.
- [81] Torbjörn Sjöstrand et al. “An introduction to PYTHIA 8.2”. In: *Comput. Phys. Commun.* 191 (2015), pp. 159–177. DOI: 10.1016/j.cpc.2015.01.024. arXiv: 1410.3012 [hep-ph].

- [82] CMS Collaboration. “Extraction and validation of a new set of CMS PYTHIA8 tunes from underlying-event measurements”. In: *Eur. Phys. J. C* 80.1 (2020), p. 4. DOI: 10.1140/epjc/s10052-019-7499-4. arXiv: 1903.12179 [hep-ex].
- [83] S. Agostinelli et al. “Geant4—a simulation toolkit”. In: *Nuclear Instruments and Methods in Physics Research Section A: Accelerators, Spectrometers, Detectors and Associated Equipment* 506.3 (2003), pp. 250–303. ISSN: 0168-9002. DOI: [https://doi.org/10.1016/S0168-9002\(03\)01368-8](https://doi.org/10.1016/S0168-9002(03)01368-8). URL: <https://www.sciencedirect.com/science/article/pii/S0168900203013688>.
- [84] CMS Collaboration. “Particle-flow reconstruction and global event description with the CMS detector”. In: *JINST* 12.10 (2017), P10003. DOI: 10.1088/1748-0221/12/10/P10003. arXiv: 1706.04965 [physics.ins-det].
- [85] Wolfgang Adam et al. *Track Reconstruction in the CMS tracker*. Tech. rep. Geneva: CERN, 2006. URL: <https://cds.cern.ch/record/934067>.
- [86] K. Rose. “Deterministic annealing for clustering, compression, classification, regression, and related optimization problems”. In: *Proceedings of the IEEE* 86.11 (1998), pp. 2210–2239. DOI: 10.1109/5.726788.
- [87] R Frühwirth, Wolfgang Waltenberger, and Pascal Vanlaer. *Adaptive Vertex Fitting*. Tech. rep. Geneva: CERN, 2007. URL: <https://cds.cern.ch/record/1027031>.
- [88] CMS Collaboration. *Technical proposal for the Phase-II upgrade of the Compact Muon Solenoid*. CMS Technical Proposal CERN-LHCC-2015-010, CMS-TDR-15-02. 2015. URL: <http://cds.cern.ch/record/2020886>.
- [89] Thomas Speer et al. *Vertex Fitting in the CMS Tracker*. Tech. rep. Geneva: CERN, 2006. URL: <https://cds.cern.ch/record/927395>.
- [90] CMS Muon POG. *Recommendations for muon related efficiencies and scale factors*. https://twiki.cern.ch/twiki/bin/view/CMS/MuonPOG#User_Recommendations. Nov. 2022.
- [91] A. Bodek et al. “Extracting Muon Momentum Scale Corrections for Hadron Collider Experiments”. In: *Eur. Phys. J. C* 72 (2012), p. 2194. DOI: 10.1140/epjc/s10052-012-2194-8. arXiv: 1208.3710 [hep-ex].
- [92] Rochester group. *Rochester corrections for muon momentum scale and resolution*. <https://twiki.cern.ch/twiki/bin/viewauth/CMS/RochcorMuon>. Nov. 2022.
- [93] CMS Luminosity POG. *recommendations (minimal, 2016–2018, RECOMMENDED)*. https://twiki.cern.ch/twiki/bin/view/CMS/LumiRecommendationsRun2#Combination_and_correlations. Nov. 2022.
- [94] CMS Collaboration. “Measurement of differential $t\bar{t}$ production cross sections in the full kinematic range using lepton+jets events from proton-proton collisions at $\sqrt{s} = 13$ TeV”. In: *Phys. Rev. D* 104.9 (2021), p. 092013. DOI: 10.1103/PhysRevD.104.092013. arXiv: 2108.02803 [hep-ex].
- [95] CMS Collaboration. “Measurement of top quark pair production in association with a Z boson in proton-proton collisions at $\sqrt{s} = 13$ TeV”. In: *JHEP* 03 (2020), p. 056. DOI: 10.1007/JHEP03(2020)056. arXiv: 1907.11270 [hep-ex].

- [96] CMS Collaboration. “Measurement of the WZ production cross section in pp collisions at $\sqrt{s} = 13$ TeV”. In: *Phys. Lett. B* 766 (2017), pp. 268–290. DOI: 10.1016/j.physletb.2017.01.011. arXiv: 1607.06943 [hep-ex].
- [97] CMS Collaboration. “Observation of the Production of Three Massive Gauge Bosons at $\sqrt{s} = 13$ TeV”. In: *Phys. Rev. Lett.* 125.15 (2020), p. 151802. DOI: 10.1103/PhysRevLett.125.151802. arXiv: 2006.11191 [hep-ex].
- [98] CMS Collaboration. “Measurements of production cross sections of the Higgs boson in the four-lepton final state in proton–proton collisions at $\sqrt{s} = 13$ TeV”. In: *Eur. Phys. J. C* 81.6 (2021), p. 488. DOI: 10.1140/epjc/s10052-021-09200-x. arXiv: 2103.04956 [hep-ex].
- [99] CMS Collaboration, Monte Carlo Generator Group. *LHE Parser in CMSSW*. <https://twiki.cern.ch/twiki/bin/view/CMS/LHEReaderCMSSW>. Nov. 2022.
- [100] Jon Butterworth et al. “PDF4LHC recommendations for LHC Run II”. In: *J. Phys. G* 43 (2016), p. 023001. DOI: 10.1088/0954-3899/43/2/023001. arXiv: 1510.03865 [hep-ph].
- [101] The ATLAS, The CMS, The LHC Higgs Combination Group Collaboration. *Procedure for the LHC Higgs boson search combination in Summer 2011*. Tech. rep. Geneva: CERN, 2011. URL: <http://cds.cern.ch/record/1379837>.
- [102] Roger Barlow and Christine Beeston. “Fitting using finite Monte Carlo samples”. In: *Computer Physics Communications* 77.2 (1993), pp. 219–228. ISSN: 0010-4655. DOI: [https://doi.org/10.1016/0010-4655\(93\)90005-W](https://doi.org/10.1016/0010-4655(93)90005-W). URL: <https://www.sciencedirect.com/science/article/pii/001046559390005W>.
- [103] J. S. Conway. “Incorporating Nuisance Parameters in Likelihoods for Multisource Spectra”. In: *PHYSTAT 2011*. 2011, pp. 115–120. DOI: 10.5170/CERN-2011-006.115. arXiv: 1103.0354 [physics.data-an].
- [104] Thomas Junk. “Confidence level computation for combining searches with small statistics”. In: *Nucl. Instrum. Meth. A* 434 (1999), pp. 435–443. DOI: 10.1016/S0168-9002(99)00498-2. arXiv: hep-ex/9902006.
- [105] A L Read. “Presentation of search results: the CL_s technique”. In: *Journal of Physics G: Nuclear and Particle Physics* 28.10 (Sept. 2002), pp. 2693–2704. DOI: 10.1088/0954-3899/28/10/313. URL: <https://doi.org/10.1088/0954-3899/28/10/313>.
- [106] Glen Cowan et al. “Asymptotic formulae for likelihood-based tests of new physics”. In: *Eur. Phys. J. C* 71 (2011). [Erratum: *Eur.Phys.J.C* 73, 2501 (2013)], p. 1554. DOI: 10.1140/epjc/s10052-011-1554-0. arXiv: 1007.1727 [physics.data-an].
- [107] Robert D. Cousins. “Generalization of Chisquare Goodness-ofFit Test for Binned Data Using Saturated Models , with Application to Histograms”. In: 2013.
- [108] Particle Data Group Collaboration. “Review of Particle Physics”. In: *PTEP* 2020.8 (2020), p. 083C01. DOI: 10.1093/ptep/ptaa104.

A Appendix

A.1 Isolation distributions

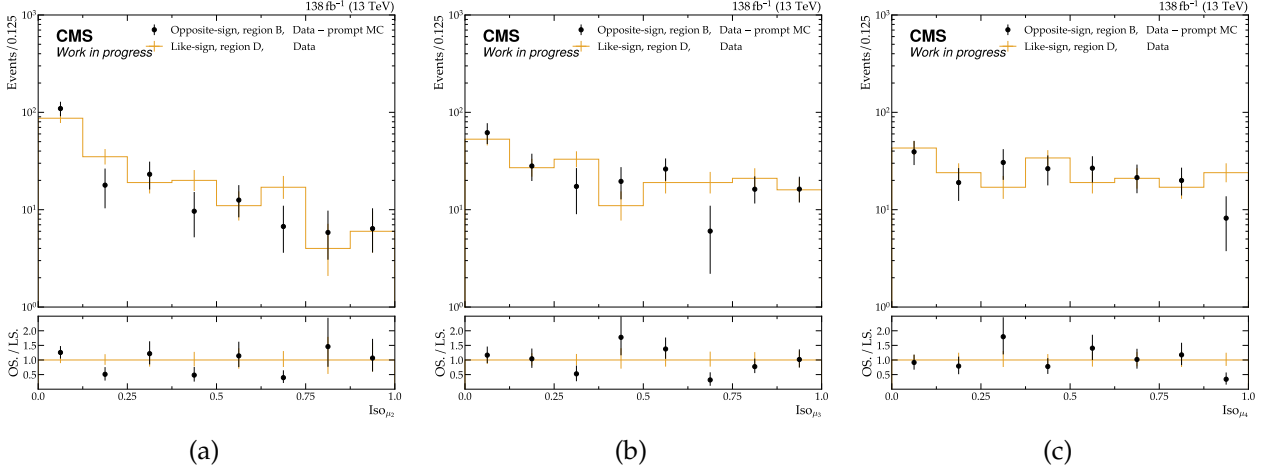


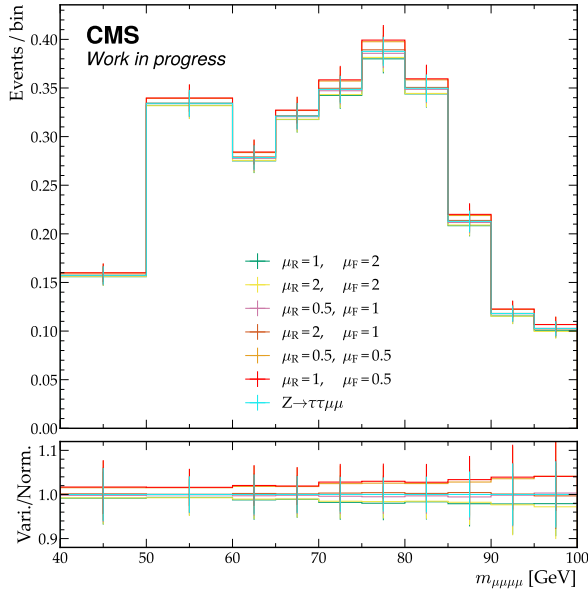
Figure 23: Distributions and statistical uncertainties of isolation variables of the three muons with lower p_T in the regions B and D.



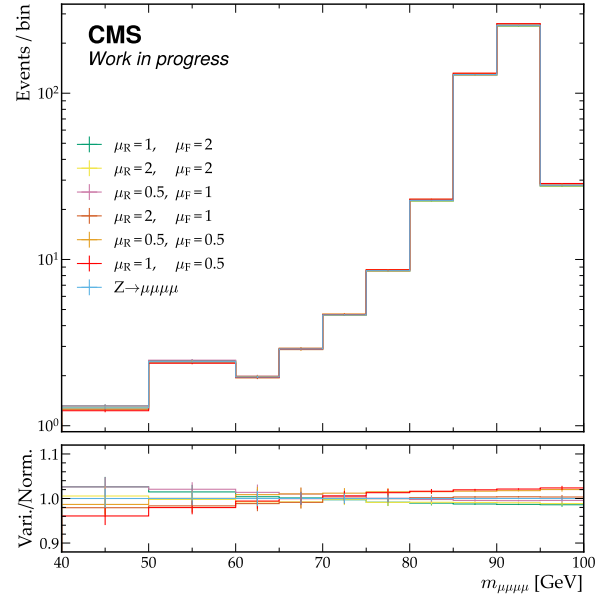
Figure 24: Distributions and statistical uncertainties of isolation variables of the three muons with lower p_T filling in the same histograms.

A.2 Systematics variations

The four muon mass distributions for the $Z \rightarrow \tau^+ \tau^- \mu^+ \mu^-$ and $Z \rightarrow \mu^+ \mu^- \mu^+ \mu^-$ obtained using the nominal and varied weights corresponding to μ_R and μ_F varied independently by 1/2 and by 2, excluding the cases where one is multiplied by 1/2 and the other by 2 are shown below.



(a)



(b)

Figure 25: Norminal and μ_R, μ_F varied four muon mass distributions for the $Z \rightarrow \tau^+\tau^-\mu^+\mu^-$ and $Z \rightarrow \mu^+\mu^-\mu^+\mu^-$ process.

The four muon mass distribution for the $Z \rightarrow \tau^+\tau^-\mu^+\mu^-$ and $Z \rightarrow \mu^+\mu^-\mu^+\mu^-$ obtained using the nominal values of all the systematics and the values shifted within each uncertainty respectively are shown in Fig 26, 27.

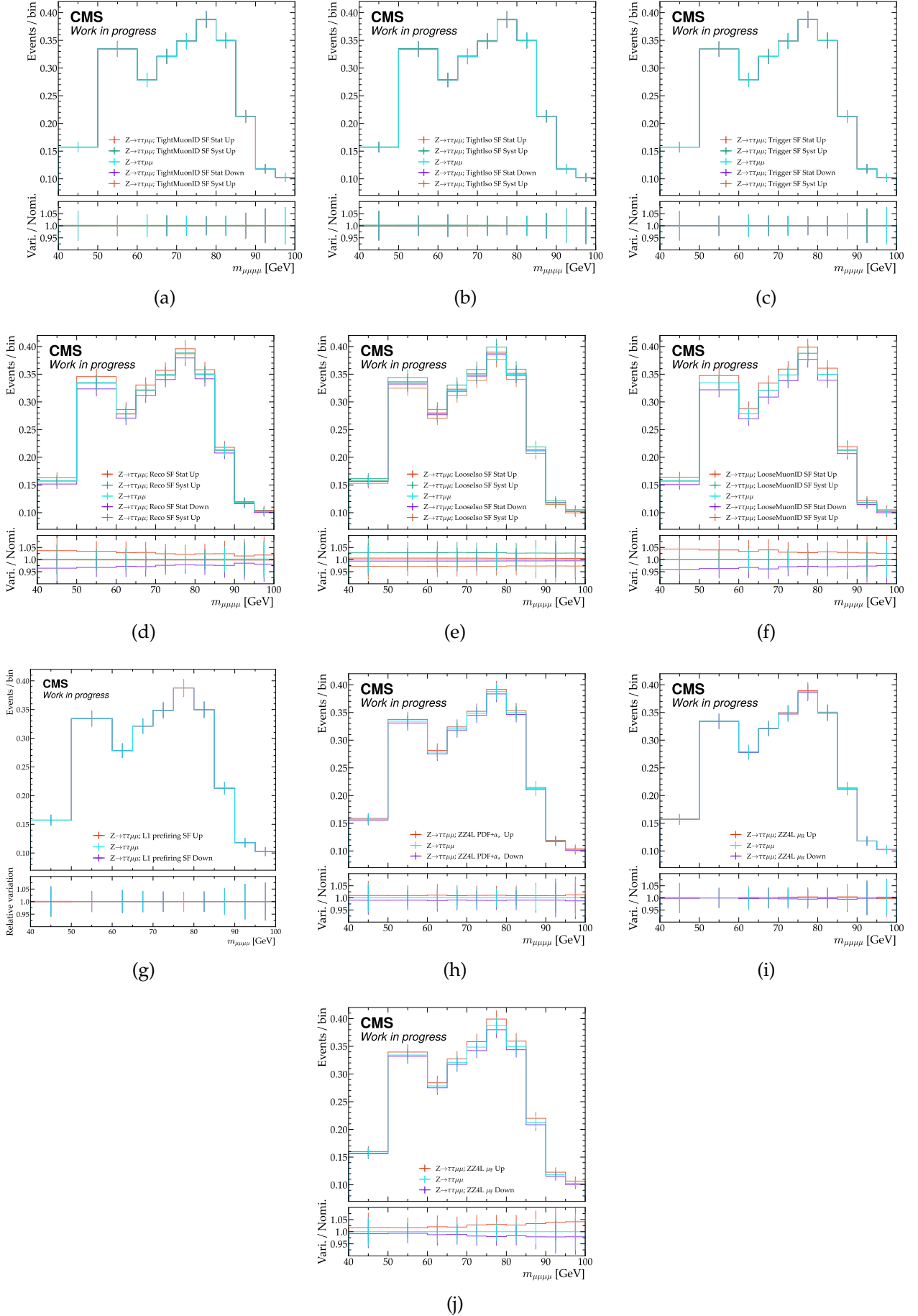


Figure 26: Norminal and varied four muon mass distributions for the $Z \rightarrow \tau^+ \tau^- \mu^+ \mu^-$ process.

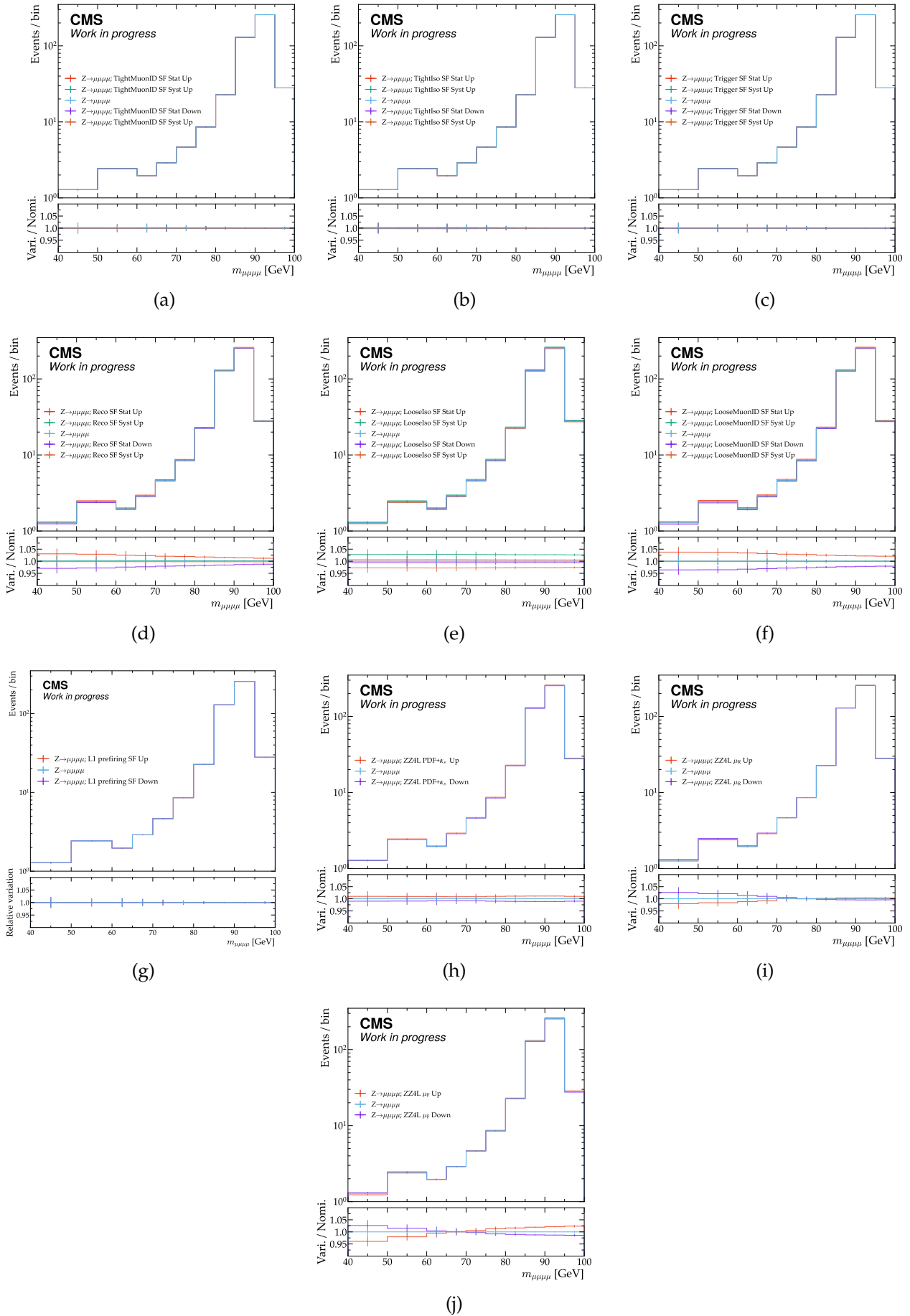


Figure 27: Normal and varied four muon mass distributions for the $Z \rightarrow \mu^+ \mu^- \mu^+ \mu^-$ process.

A.3 Acceptance and efficiencies cross check

The acceptance A and efficiencies ϵ for the $Z \rightarrow \tau^+\tau^-\mu^+\mu^-$ and $Z \rightarrow \mu^+\mu^-\mu^+\mu^-$ processes, obtained from simulation using the ZZTo4LM-1toInf samples for cross check.

Table 13: Efficiency and acceptance of the two decay modes per year of data taking.

Year	$A_{Z \rightarrow \mu^+\mu^-\mu^+\mu^-}$	$\epsilon_{Z \rightarrow \mu^+\mu^-\mu^+\mu^-}$	$A_{Z \rightarrow \tau^+\tau^-\mu^+\mu^-}$	$\epsilon_{Z \rightarrow \tau^+\tau^-\mu^+\mu^-}$
2016 preVFP	0.1638 ± 0.0010	0.3982 ± 0.0033	0.0610 ± 0.0041	0.2794 ± 0.0300
2016 postVFP	0.1705 ± 0.0011	0.4067 ± 0.0034	0.0694 ± 0.0045	0.2821 ± 0.0295
2017	0.1540 ± 0.0007	0.3748 ± 0.0024	0.0487 ± 0.0025	0.1869 ± 0.0204
2018	0.1708 ± 0.0006	0.3885 ± 0.0018	0.0677 ± 0.0024	0.2041 ± 0.0145

A.4 Additional kinematic distributions

Various kinematic distributions are shown. They are determined by the fit on the invariant mass of the four muons. Below the four muons in the event are ordered by p_T .

Signal plus background pre-fit distributions

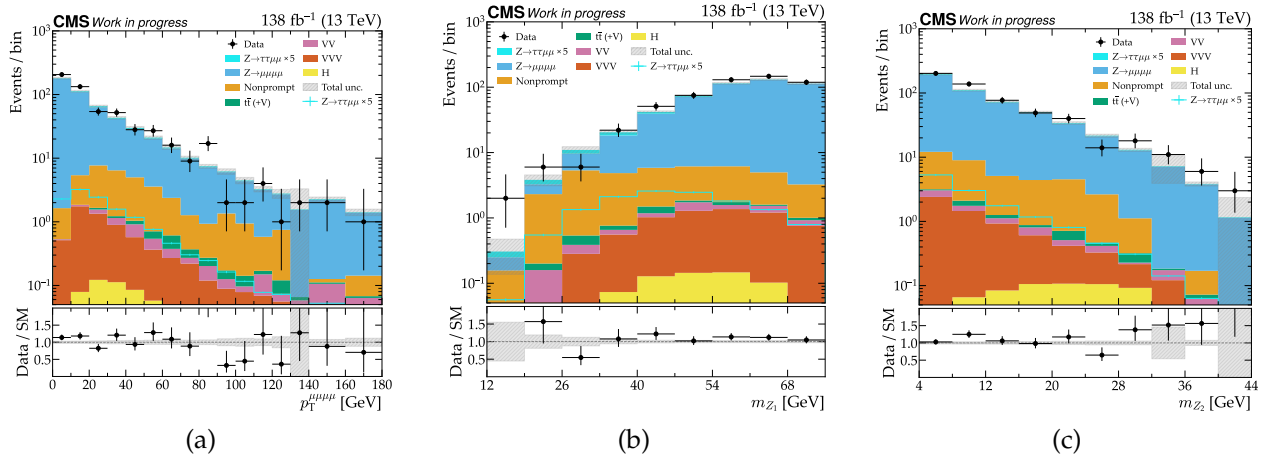


Figure 28: Signal plus background pre-fit distributions for (a) the p_T of the four muon system, (b) the mass of Z_1 , (c) the mass of Z_2 .

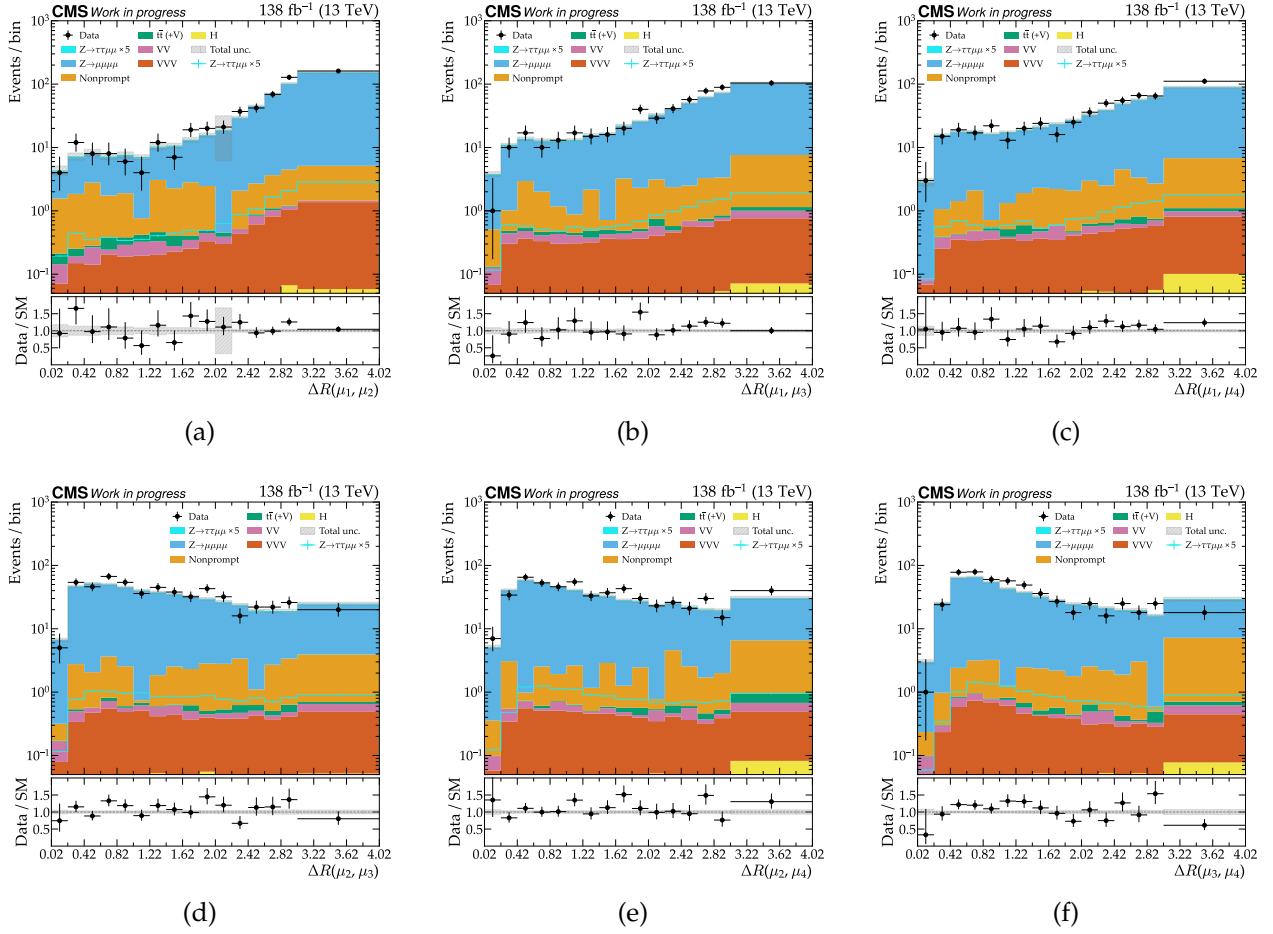


Figure 29: Signal plus background pre-fit distributions for the distance ΔR between each muon pairs.

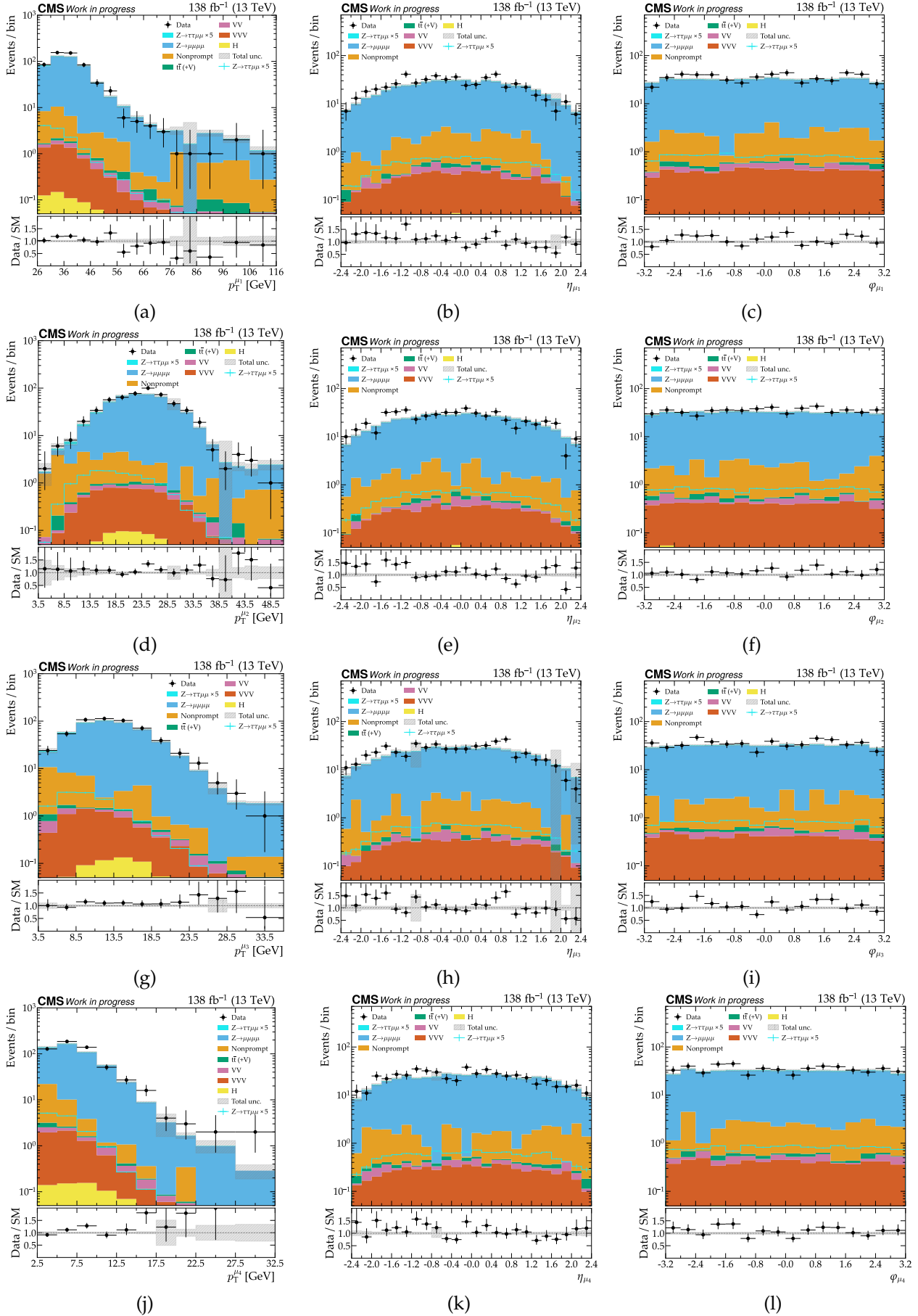


Figure 30: Signal plus background pre-fit distributions for the p_T , η , ϕ of each muon.

Background-only post-fit distributions

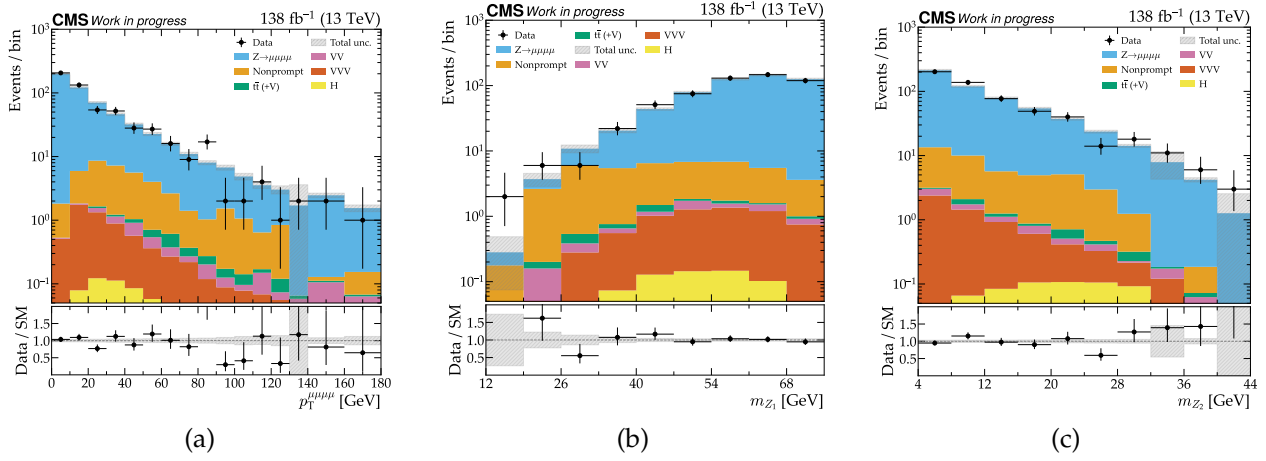


Figure 31: Background post-fit distributions for (a) the p_T of the four muon system, (b) the mass of Z_1 , (c) the mass of Z_2 .

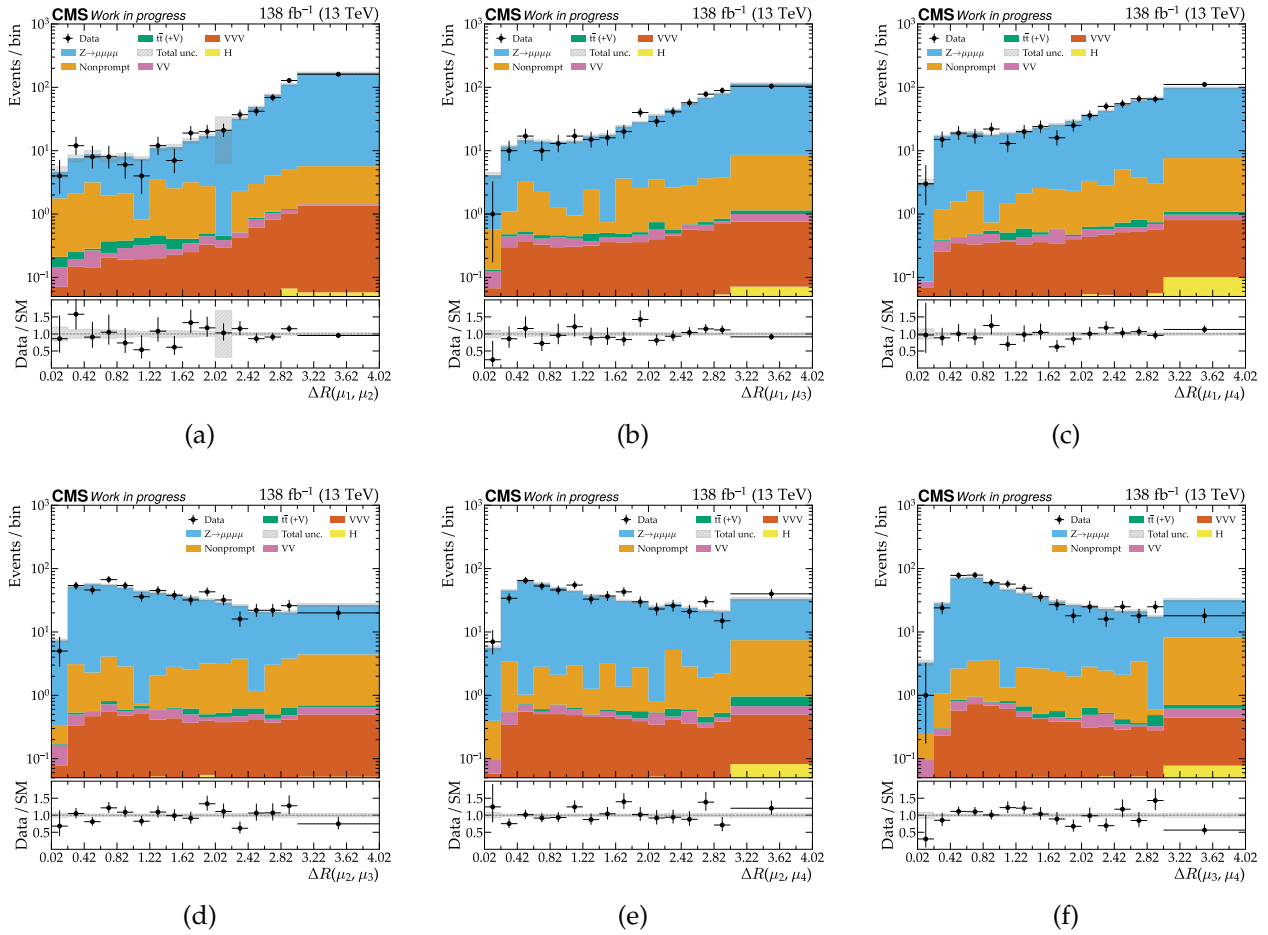


Figure 32: Background only post-fit distributions for the distance ΔR between each muon pairs.

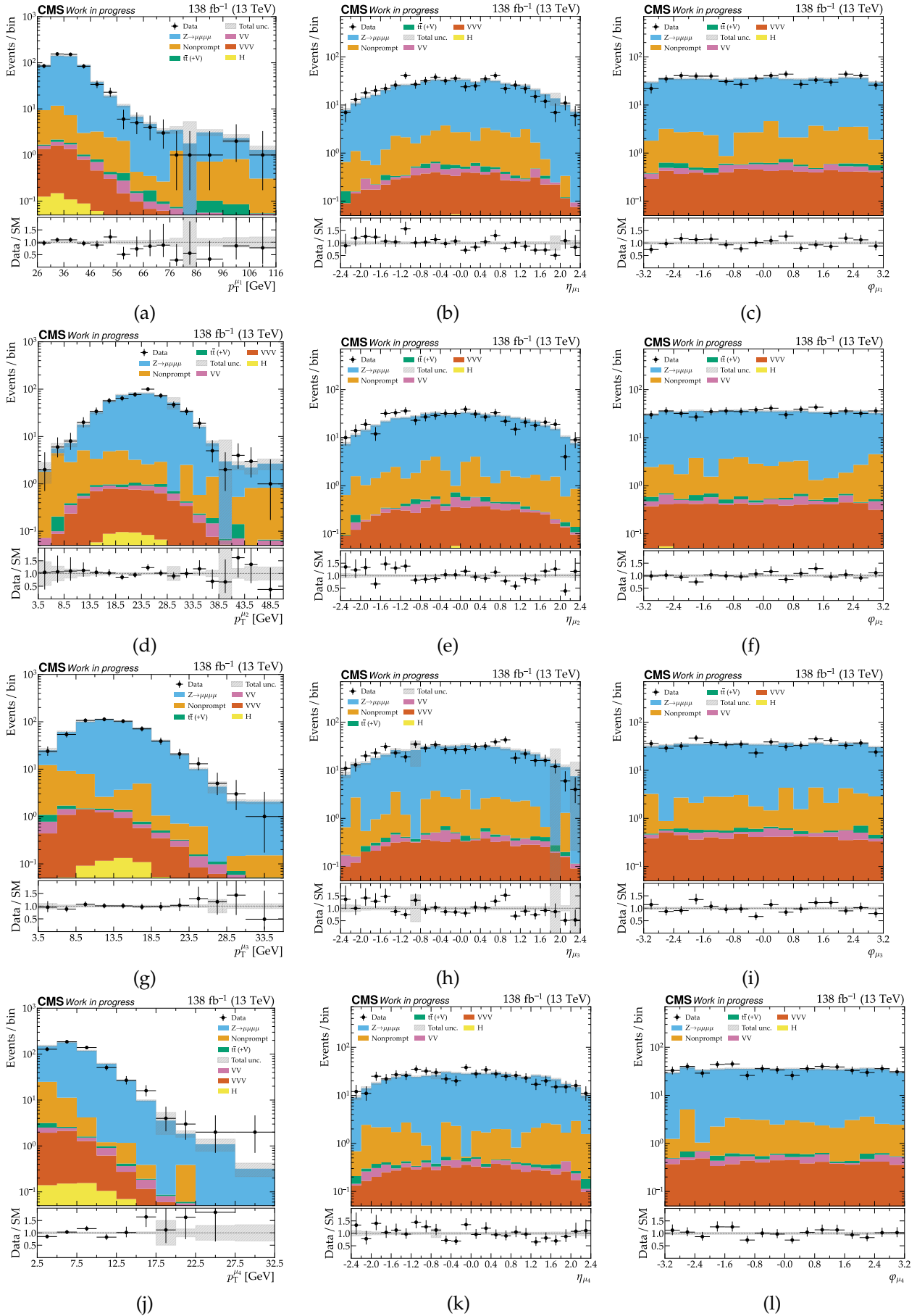


Figure 33: Background only post-fit distributions for the p_T , η , ϕ of each muon.